JGR Planets

RESEARCH ARTICLE
10.1029/2022JE007723

Key Points:

- Erosion and deposition follow the subsolar latitude and are strongly influenced by local topography
- Scarp activity is primarily limited to equatorial and internal regions
- We observe net zero erosion/deposition on the tops of the lobes, perhaps indicating the presence of terminal sinks for airfalling sediment

Supporting Information:

Supporting Information may be found in the online version of this article.

Correspondence to:

M. N. Barrington,
mne8@cornell.edu

Citation:

Barrington, M. N., Birch, S. P. D., Jindal, A., Hayes, A. G., Corlies, P., & Vincent, J.-B. (2023). Quantifying morphological changes and sediment transport pathways on comet 67P/Churyumov-Gerasimenko. *Journal of Geophysical Research: Planets*, *128*, e2022JE007723. https://doi.org/10.1029/2022JE007723

Received 17 DEC 2022
Accepted 20 JUN 2023
Corrected 24 AUG 2023

This article was corrected on 24 AUG 2023. See the end of the full text for details.

Author Contributions:

Conceptualization: S. P. D. Birch, A. G. Hayes
Methodology: S. P. D. Birch, A. Jindal, A. G. Hayes, P. Corlies
Software: J.-B. Vincent
Supervision: A. G. Hayes
Validation: A. Jindal, A. G. Hayes
Writing – review & editing: S. P. D. Birch, A. Jindal, A. G. Hayes, P. Corlies, J.-B. Vincent

Quantifying Morphological Changes and Sediment Transport Pathways on Comet 67P/Churyumov-Gerasimenko

M. N. Barrington[1], S. P. D. Birch[2,3], A. Jindal[3], A. G. Hayes[3], P. Corlies[2,3,4], and J.-B. Vincent[5]

[1]Department of Earth and Atmospheric Sciences, Cornell University, Ithaca, NY, USA, [2]Department of Earth, Atmospheric, and Planetary Sciences, Massachusetts Institute of Technology, Cambridge, MA, USA, [3]Department of Astronomy, Cornell University, Ithaca, NY, USA, [4]Now at Spectral Sciences Inc., Burlington, MA, USA, [5]DLR Institute of Planetary Research, Berlin, Germany

Abstract Comets are active geological worlds with primitive surfaces that have been shaped to varying degrees by sublimation-driven sediment transport and mass wasting processes. Rosetta's rendezvous with comet 67P/Churyumov-Gerasimenko (67P) in 2014 provided data with the necessary spatial and temporal resolutions to observe many evolutionary processes on micro-gravity worlds. Rosetta's observations have thus far revealed that many changes to the surface occurred within 67P's smooth terrains, vast sedimentary deposits that blanket a significant fraction of the nucleus. Understanding the global context of these changes, and therefore the sediment transport pathways that govern the evolution of 67P's surface, requires a thorough description of their changing morphologies and an evaluation of existing global-scale spatial and temporal trends. Accordingly, we present a time-resolved synthesis of erosion and deposition activity on comet 67P as it passed through its 13 August 2015 perihelion from September 2014 to August 2016. Our mapping results indicate that, around perihelion, sediment is globally redistributed inter-regionally from 67P's more active south to the north. Equally important, however, are local, topographically influenced sediment transport processes, with large volumes of sediment moving intra-regionally over sub-kilometer distances. We also show evidence for regions of near-zero net erosion/deposition between approximately 30°N–60°N latitude, which may act as terminal sedimentary sinks, with the remobilization of these materials hindered by multiple factors. Our work therefore provides the most complete mapping of sediment transport processes and pathways across 67P, a critical step toward understanding the global landscape evolution of both 67P and other comets.

Plain Language Summary Comets are some of the oldest materials in the solar system. When these ice-rich bodies approach the sun, the ice at the surface can sublimate, breaking down solid materials into sediment that can be mobilized across and off of the comet's surface. On comet 67P, sublimated vapor can move material in many ways. Determining how and where materials move across this comet can help us understand how its ice content has changed since it formed and how other comet surfaces may change over time. We found that the location and timing of sediment transportation are linked to the location of most direct sunlight on the comet's surface. Additionally, we only observed migrating scarps of smooth materials in either outer, equatorial regions of the comet or within "internal" regions that receive extra heat from the comet itself. We also found that sediments moved within and between regions after their initial deposition. However, we observed almost no sediment transport on the top of either lobe, perhaps indicating that the amount of deposited material is limited and may not be easily eroded after deposition. We predict that the processes transporting sediments on 67P will affect comets of similar orbits and masses.

1. Introduction

Comets are composed of primitive materials that once existed frozen in the outer realm of the solar system. These remnants of the earliest era of planetary formation were eventually transported to their current reservoirs through planetary migration and/or interactions with other stars and gas clouds (A'Hearn et al., 2012). While these objects have undergone significant processing before entering their current reservoirs (Lisse et al., 2022; Steckloff et al., 2023), they represent some of the least processed materials in the solar system. Jupiter Family Comets (JFCs) are of particular interest for scientific study due to their short orbital periods, and close perihelion passages that permit detailed spacecraft observations. Broadly, as these objects migrated increasingly closer to the Sun, their volatile-rich surfaces began to evolve as various ices exposed at the surface sublimated. This

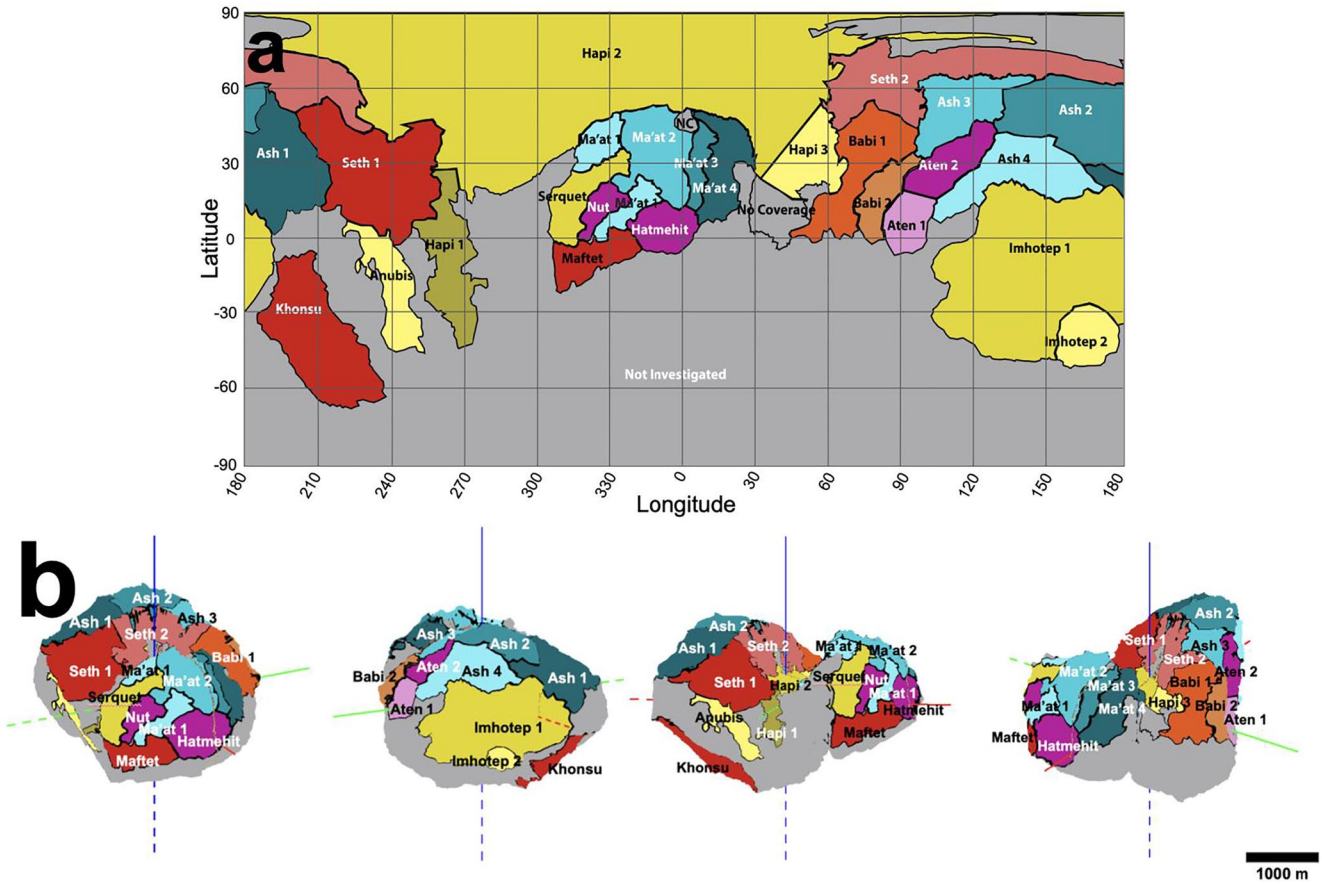

Figure 1. (a) An equirectangular projection of our 25 sub-regions of smooth terrains analyzed for surface evolution. Colored regions are dominated by smooth terrains, while the regions in gray show few smooth terrains, instead being dominated by consolidated materials. Gray regions were not considered in our work. Regions labeled "No Coverage" and "NC" were not investigated due to insufficient coverage in reference images. (b) Four orientations of a 3D projection of 25 sub-regions of smooth terrains on 67P. *X*-Axis: Red, *Y*-Axis: Green, *Z*-Axis: Blue. Dashed lines represent negative axis directions.

process drives the physical and chemical weathering of the consolidated nucleus, wherein sediment is produced and transported either across, or entirely ejected from, the nucleus.

To date, five JFCs visited by spacecraft observations have been sufficiently resolved to permit geological studies of their surfaces. These include 19P/Borrelly (Britt et al., 2004; Sodorblom et al., 2002), 81P/Wild 2 (Brownlee et al., 2004; Tsou et al., 2004), 9P/Tempel 1 (P. C. Thomas et al., 2013a; Veverka et al., 2013), 103P/Hartley 2 (P. C. Thomas et al., 2013b), and 67P/Churyumov-Gerasimenko (67P) (El-Maarry et al., 2017). These observations all showed that cometary nuclei are complex worlds, with regions of unconsolidated sedimentary grains coating an otherwise consolidated, rugged nucleus (Sunshine et al., 2016). Observations of comet 1P/Halley (Reinhard, 1986), though hinting at similar landscapes, had insufficient resolutions for more quantitative analyses.

Of these five JFCs, the highest spatial and temporal resolution data sets documented comet 67P. Rosetta collected over 8,200 high resolution images of 67P's surface over the span of the mission's 2 year visit to the comet from 2014 to 2016 (Keller et al., 2007). These data provide a unique opportunity to observe high spatial and temporal resolution changes occurring on 67P's smooth terrains. Here, the term smooth terrains is used as a catch-all term to describe morphologies which have previously been described as smooth terrains, cauliflower plains, and pitted plains on comet 67P (Birch et al., 2017). Smooth terrains are composed of sedimentary grains that are likely sourced from the consolidated nucleus, albeit by unknown means. Sublimation of ice within the consolidated nucleus then weathers the nucleus, accelerating liberated particles off the surface. Larger grains then follow ballistic trajectories and fall back to the surface, depositing as "airfall" in topographical and gravitational lows in the comet's northern latitudes (Figure 1; Keller et al., 2017). Airfall grain sizes range from centimeter to decimeter scale (Keller et al., 2017) and are heterogeneous in both their size distribution (Pajola et al., 2017) and volatile

content (Davidsson et al., 2021) across the surface of 67P. While it was initially hypothesized that these airfall materials would act as an insulating layer that would suppress activity from the more ice-rich layers below (Keller et al., 1986), Rosetta instead observed that the smooth terrains hosted the majority of large-scale changes. This suggests that the sedimentary grains retain large volumes of volatile ices despite their exposure within the coma during transport. Indeed, Davidsson et al. (2021) found that for a transit time of 12 hr, centimeter-sized particles retained ~50% of their original water ice, with decimeter sized particles retaining up to ~90%. More volatile ices (e.g., CO, CO_2), however, are depleted well within typical transit times (Davidsson et al., 2021).

Past work has documented several types of morphological units on 67P, including consolidated nucleus materials, which often outcrop in the form of cliffs within smooth terrain regions, as well as bouldered terrains, talus deposits, smooth terrains, cauliflower plains, and pitted plains (Birch et al., 2017). Surface changes that have been examined in detail include depressions (Birch et al., 2017), scarps (Birch et al., 2017; El-Maarry et al., 2017; Jindal et al., 2022), honeycomb features (El-Maarry et al., 2019; Hu et al., 2017; Shi et al., 2016), ripples (El-Maarry et al., 2017; Jia et al., 2017), pits (Deshapriya et al., 2016), and bright spots (Deshapriya et al., 2016; Fornasier et al., 2015). Although these many studies documented the evolution of isolated regions and features on 67P, a synthesis of the evolution of all of 67P's smooth terrains has remained unexplored. Thus, it is necessary to study the global geologic processes which have acted on 67P, a task that will have broad implications for cometary surfaces more generally. Herein, we present a synthesis of the sublimation-driven surface evolution and sediment redistribution of the smooth terrains of comet 67P. Our work has three primary objectives: (a) to detect and classify meter to decameter scale sublimation-driven changes in the smooth terrains of comet 67P, (b) to categorize these changes as either erosion, deposition, or redistribution of sediment, and (c) to synthesize the complex spatial and temporal trends in these categories of sediment transport with respect to 67P's orbital parameters. We use these data to discuss how observed trends in sediment transport on 67P apply to other comets and possible future comet missions.

2. Methods

We utilized images collected by Rosetta's Optical, Spectroscopic, and Infrared Remote Sensing Imaging System (OSIRIS) Narrow Angle Camera (NAC), which acquired over 8,200 images of the surface of comet 67P. These data document both the coma and the surface of the comet before, during, and after 67P's 2015 perihelion passage. Previous mapping of 67P (El-Maarry et al., 2015; N. Thomas et al., 2015b) documented smooth terrain deposits across the comet, with most deposits found in 67P's northern hemisphere (Birch et al., 2017; El-Maarry et al., 2015). For portions of the comet containing known smooth terrains, we divided them into 25 distinct sub-regions, with naming conventions based on the nomenclature from El-Maarry et al. (2015) (Figure 1). This subdivision was done out of necessity because of (a) the comet's complex geometry, (b) data quality variations, (c) data coverage gaps, and (d) the vast latitudinal and longitudinal expanse of several previously defined (El-Maarry et al., 2015) regions. Despite various attempts to generate an automated image processing pipeline, we determined that manual image selection was the most efficient way to find images that: (a) met resolution requirements, (b) displayed a significant portion of a given region under investigation, (c) did not display locally saturated data, and (d) provided optimal viewing geometry and phase angles for the detection of 1–10 m scale changes. To reduce errors in change detection due to variations in viewing geometry, phase angles between 45° and 90° were preferentially selected for image analysis, with >90% of images falling within this range (Table S1). Due to inconsistent coverage of each region, more extreme phase angles were also utilized as necessary when higher quality observations were not available (Table S1).

Our method of manual image selection, projection, and change detection was performed in multiple steps. First, reference images were manually selected for each sub-region as early as data coverage of each region allowed. Next, follow-up images of each sub-region were selected, initially at a cadence of once per month after the date of their respective reference images. If changes were detected between two consecutive images at this cadence, the image cadence was increased systematically until either no further changes were detected between consecutive images or until coverage of the region was not available at a shorter interval of time. Whenever possible, we leverage multiple images of a given surface change, though sporadic coverage and changing resolution/imaging conditions meant such confirmations, as well as precise determinations about the dates on which changes began/ceased were not always possible (yellow boxes in Table S3).

For each sub-region, we then projected each image into the frame of our reference image using the ShapeViewer (www.comet-toolbox.com) software (Vincent et al., 2018). This allowed us to blink images and more reliably detect finer-scale changes and their precise locations than what would otherwise be possible by analyzing

unprojected images side-by-side. ShapeViewer also allowed for viewing high-resolution, small field-of-view images in a global context, aiding in our later interpretations. Finally, for each region, mapping of all changes was performed in the ArcGIS software as shapefiles and layers. Identified changes, each confirmed by at least two individual mappers, were annotated and analyzed for 619 images in total (Table S1) with resolutions ranging from approximately 0.1–20 m/pixel. If necessary, the contrast and brightness of each image were adjusted to provide a better perspective for the interpretation of possible changes in each image. Measurements of distance and feature size were made in ArcMap by converting an arbitrary unit to meters using scale bars created during layer generation in ShapeViewer. We obtained subsolar latitude values over each time bin (Figure 6) using the Navigation and Ancillary Information Facility (NAIF) SPICE toolkit (Acton, 1996).

It is important to note that data coverage was incomplete, especially near perihelion from mid- to late-2015 as the Rosetta spacecraft backed away from the comet. This resulted in images having far coarser resolution during these most active periods. Images also had variable phase angles and illumination conditions, further complicating our search for changes. For example, data over 67P's northern latitudes were progressively more difficult to use, eventually becoming unusable when those latitudes entered polar winter (black boxes in Table S3). Resolution limitations were addressed first by including estimated uncertainties (yellow boxes, Table S3) between dates when changes were observed and the earliest date a change may have occurred before our observation. Next, wherever possible, observations were confirmed in sequential images. Whenever a candidate change was unclear due to poor resolution, the changes were flagged as "low-confidence" observations (Table S2), and were not included in the synthesis of activity in the northern hemisphere. Sequential images whose average phase angles vary by more than 45° were also flagged in Table S1. Therefore, while we know our mapping is incomplete near perihelion and for scales below ∼1 m, our consistent image selection, projection, and stretching routine allowed us to place constraints on when we were certain that activity occurred in a given region (green boxes in Table S3) and when it was possible, but not confirmed, that activity occurred (yellow boxes in Table S3). We accordingly specify that observations occur by a specific date to indicate the latest possible date on which a change occurred, as limited by either resolution, shadows, viewing geometry, or data coverage.

We identified and searched for six types of changes in each of our 25 sub-regions. These changes included boulder burial, boulder exposure, boulder migration, scarp migration (Figure 2), plains migration (Figure 3), and honeycomb evolution (Figure 4). See Table S2 for a complete catalog of detected changes. For the purposes of our work, boulder burial includes only boulders that were completely covered by the deposition of new smooth terrains (Figure 2), as varying illumination conditions and distortions inherent to the projection of images complicated our ability to interpret any partial burials. Boulder exposure likewise describes boulders which had been completely covered by smooth terrains and were later revealed, but does not include already exposed boulders undergoing further local erosion for the same reasons as above (Figure 2). Exposures and burials of outcrops of the underlying consolidated nucleus were interpreted similarly to their boulder counterparts and were classified in these same categories for simplicity. Boulder migration documents the movement of boulders ranging from meters to tens of meters in diameter within talus deposits and boulder fields, falling from local cliffs, or those being emplaced from regions beyond individual image boundaries (i.e., the initial boulder location is not known). Differentiation between boulder exposures and boulder migrations was typically made based on two factors: (a) Previous indication(s) of a boulder's presence. Visible evidence of boulders beneath the surface sediment, such as mounds of sediment where a boulder is later exposed, are all classified as boulder exposures. (b) The boulder's proximity to talus deposits. If the pre-existing location of a boulder cannot be determined, the boulder is classified as migration when located within or proximal to a talus deposit. If distal from any talus deposit or cliff within the center of a smooth terrain deposit, we instead classify it as boulder exposures. One exception is the ∼10 m scale boulder that migrated from an unknown cliff into Hapi 1 (Figure 2), distinguished by slight impact impressions near the new boulder in the center of the region.

Scarp migration describes the formation and/or subsequent movement of arcuate or semi-arcuate depressions (Figure 2), all of which are bounded at least on one side by a migrating scarp wall. These depressions are typically observed migrating radially from a topographic discontinuity, although the genesis point is not always clear (Birch et al., 2019; Jindal et al., 2022). The radial migration of the scarps is key in differentiating between the processes of scarp migration and plains migration.

Plains migration describes the redistribution of sediment deposits which form mounds or dune-like crests (Figure 3; N. Thomas et al., 2015a). We detected this process by analyzing the movement of these mounds

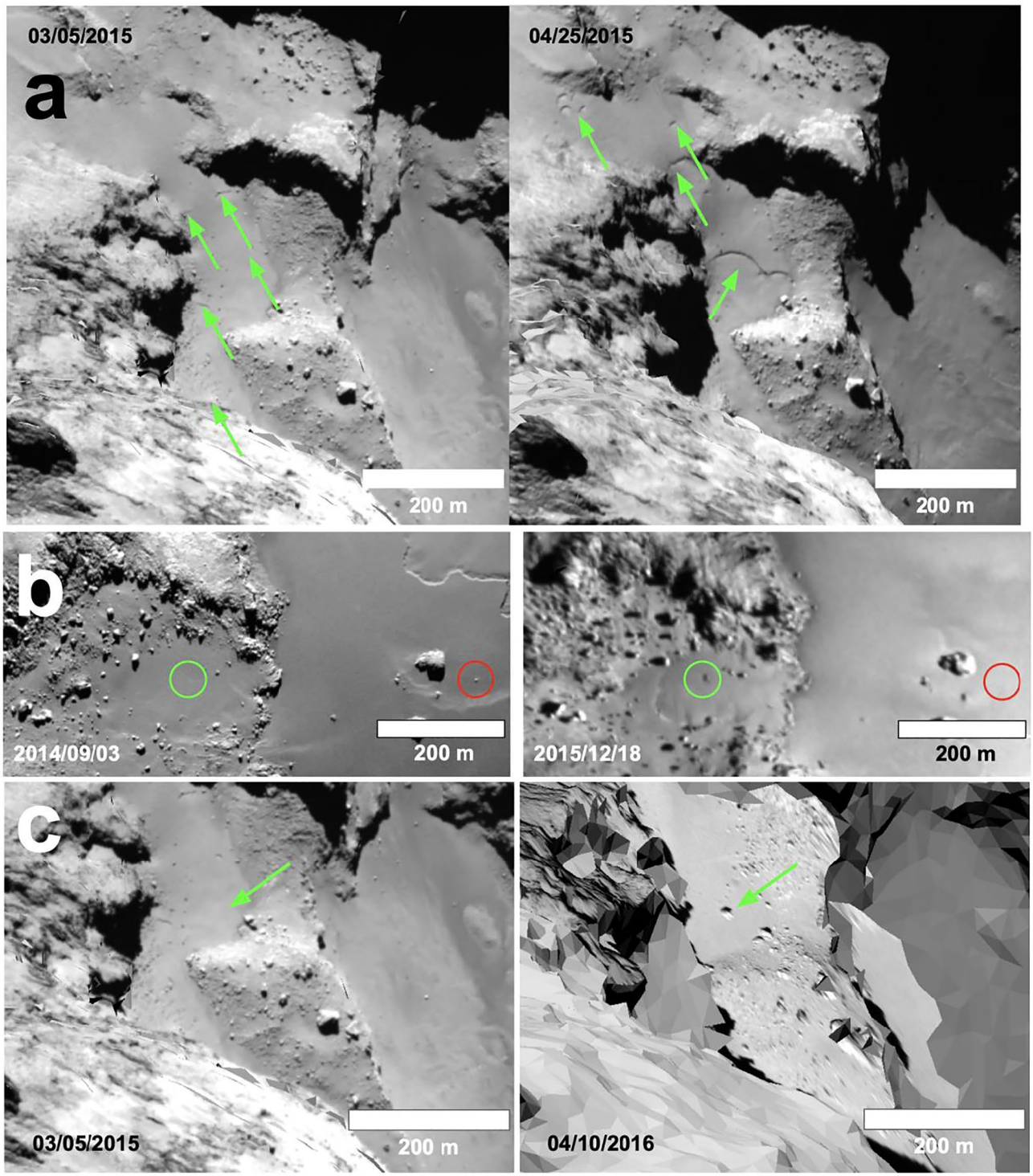

Figure 2. (a) Co-registered images of Hapi 1 showing arcuate scarp fronts migrating (green arrows) between 5 March and 25 April 2015. (b) One boulder exposure circled in green and one boulder burial circled in red, seen in Imhotep 1. (c) One boulder sourced from an unknown location migrating into Hapi 1.

and crests, identifying variations in surface roughness, and/or observing changing locations of the boundaries between smooth terrains and neighboring consolidated regions.

Finally, honeycomb evolution describes the increase or decrease in the surface roughness of "honeycombs" (El-Maarry et al., 2019; Hu et al., 2017; Shi et al., 2016). These decameter scale, highly textured areas form just

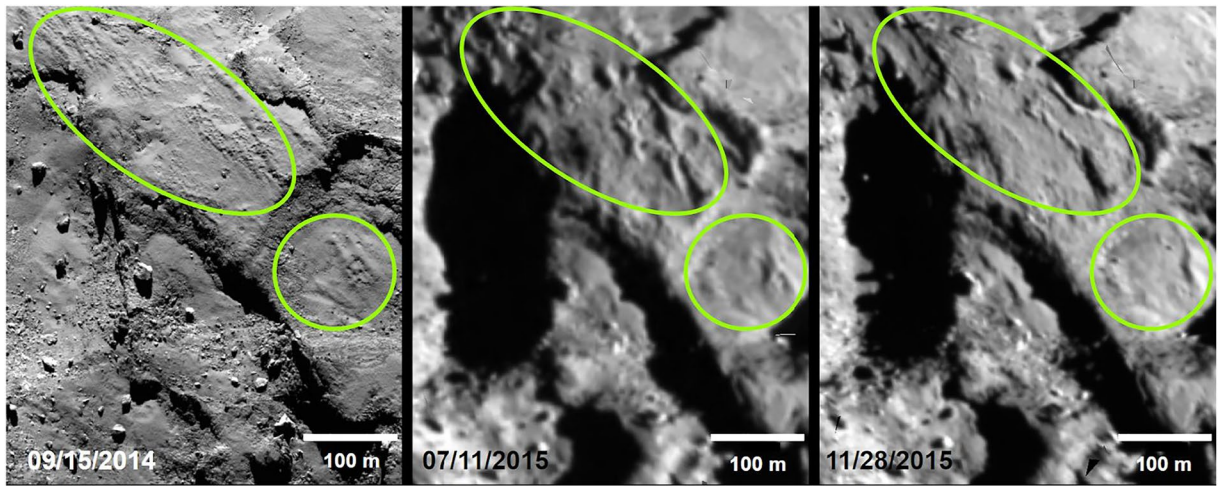

Figure 3. Co-registered images showing migrating sediment plains in Maftet.

beneath some smooth terrains. As such, they experience a reduction in surface roughness when new granular materials are deposited, and an increase in roughness when overlying material is eroded (Figure 4; Shi et al., 2016).

In addition to the six broad types of changes described above, several additional isolated types of changes were observed throughout the mission. These include the formation of bright, likely ice-rich, pits in Khonsu (Figure 5; Deshapriya et al., 2016; Fornasier et al., 2015; Oklay et al., 2016), the destruction and subsequent reformation of a set of ripple bedforms in Hapi 1 (Figure S1 in Supporting Information S1; El-Maarry et al., 2017; Jia et al., 2017), and quasi-circular pits that appear in Ash 1.

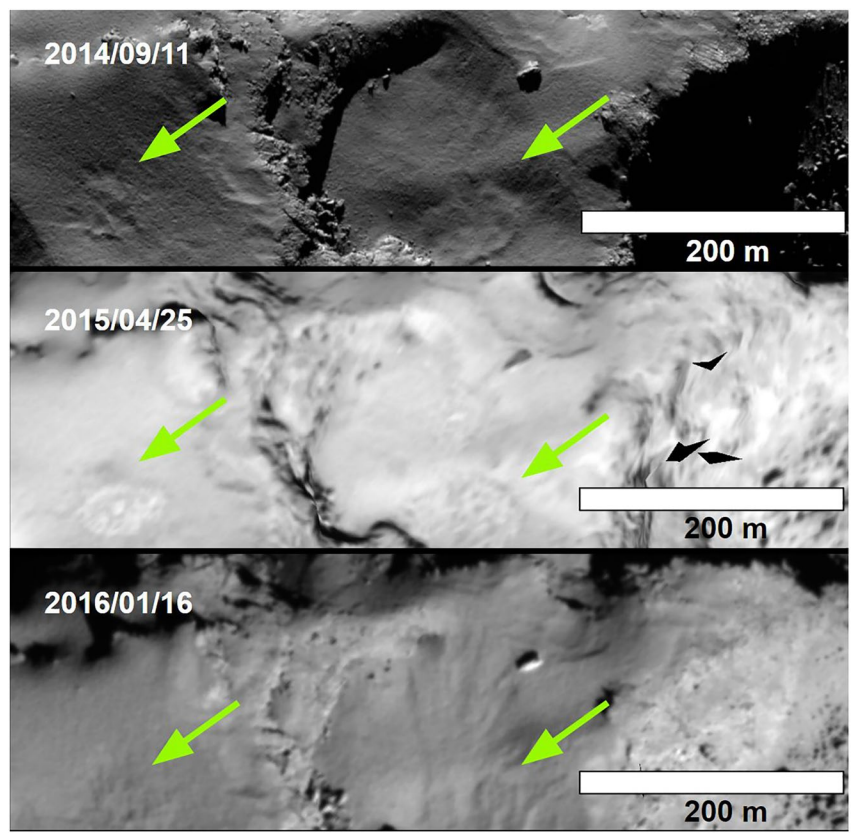

Figure 4. Co-registered images showing evolving honeycomb structures in Seth 1.

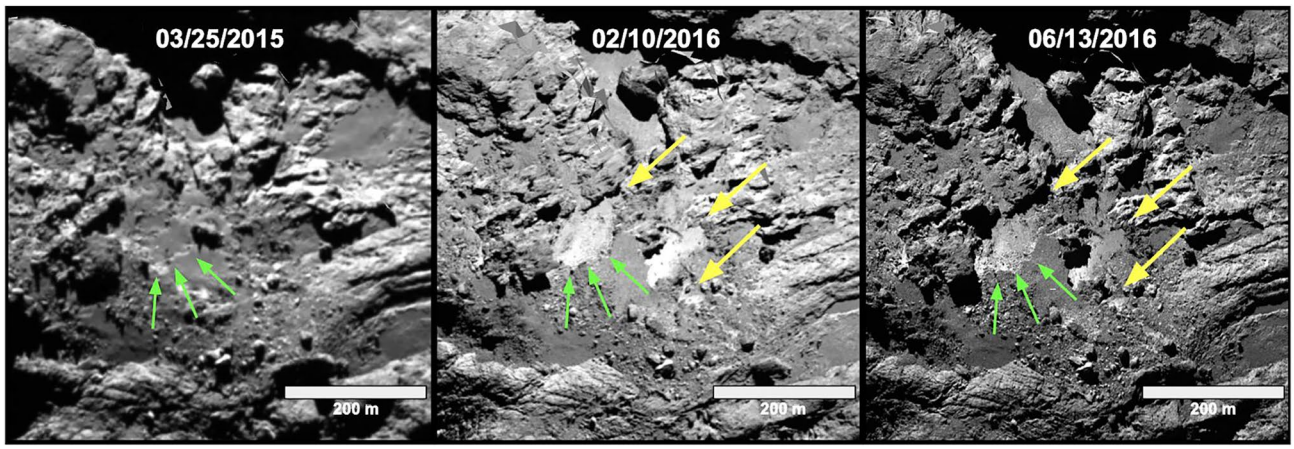

Figure 5. Co-registered images documenting the evolution of bright pits in Khonsu. (left) No bright pits were present on 25 March 2015, although some pre-existing structure that created the left pit's boundary can be seen (green arrow). The location of future bright pits is covered under a dust mantle. (center) The dust mantle has been eroded to reveal two ~100 m scale bright pits, and one 10 m scale bright pit as seen on 10 February 2016 (green arrows indicate the left pit's structural boundary, yellow arrows indicate locations of bright spots). (right) The bright pits are still visible on 13 June 2016 (yellow arrows) but they have exhibited an overall reduction in brightness.

We classified each type of change into categories of erosion, deposition, or re-distribution for the synthesis of global sediment transport trends and sorted changes into 3-month time bins (Table S3; Figures 7–9). Scarp migration, boulder/nucleus exposure, boulder migration, increased surface roughness in honeycombs, and pit formation in Ash and Khonsu are all classified as erosional processes. All these processes act to remove granular smooth terrain material on the surface, most likely driven by the sublimation of near-surface volatile ices (Birch et al., 2019; El-Maarry et al., 2017; Hu et al., 2017; Jindal et al., 2022). We classify boulder burials, nucleus burials, and decreased surface roughness of honeycombs as indicators of deposition of new smooth terrain sediment. While other research classifies the burial of scarps as a depositional indicator (Jindal et al., 2022), we did not include them here due to the difficulty of classifying fading scarps with varying viewing geometries. However,

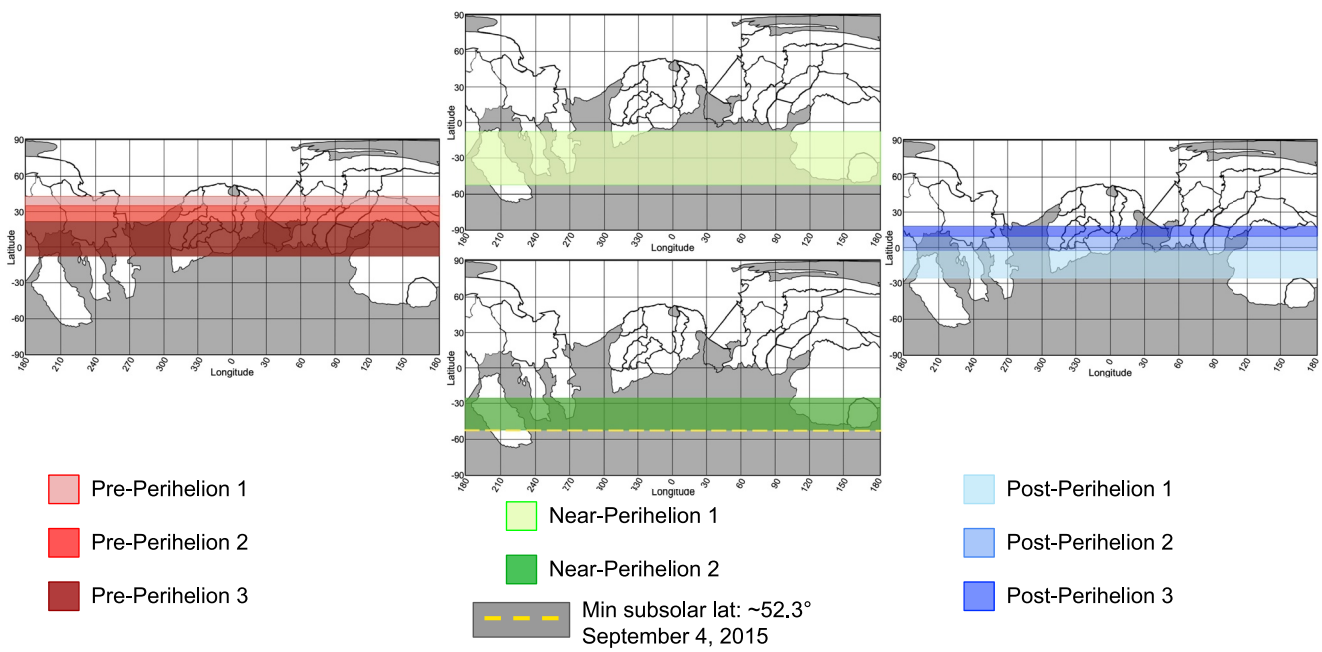

Figure 6. Equirectangular projection indicating the ranges of the subsolar latitude over the span of each time bin. Pre-perihelion time bins are shown in shades of red (left), near-perihelion time bins in shades of green (center), and post-perihelion time bins in shades of blue (right).

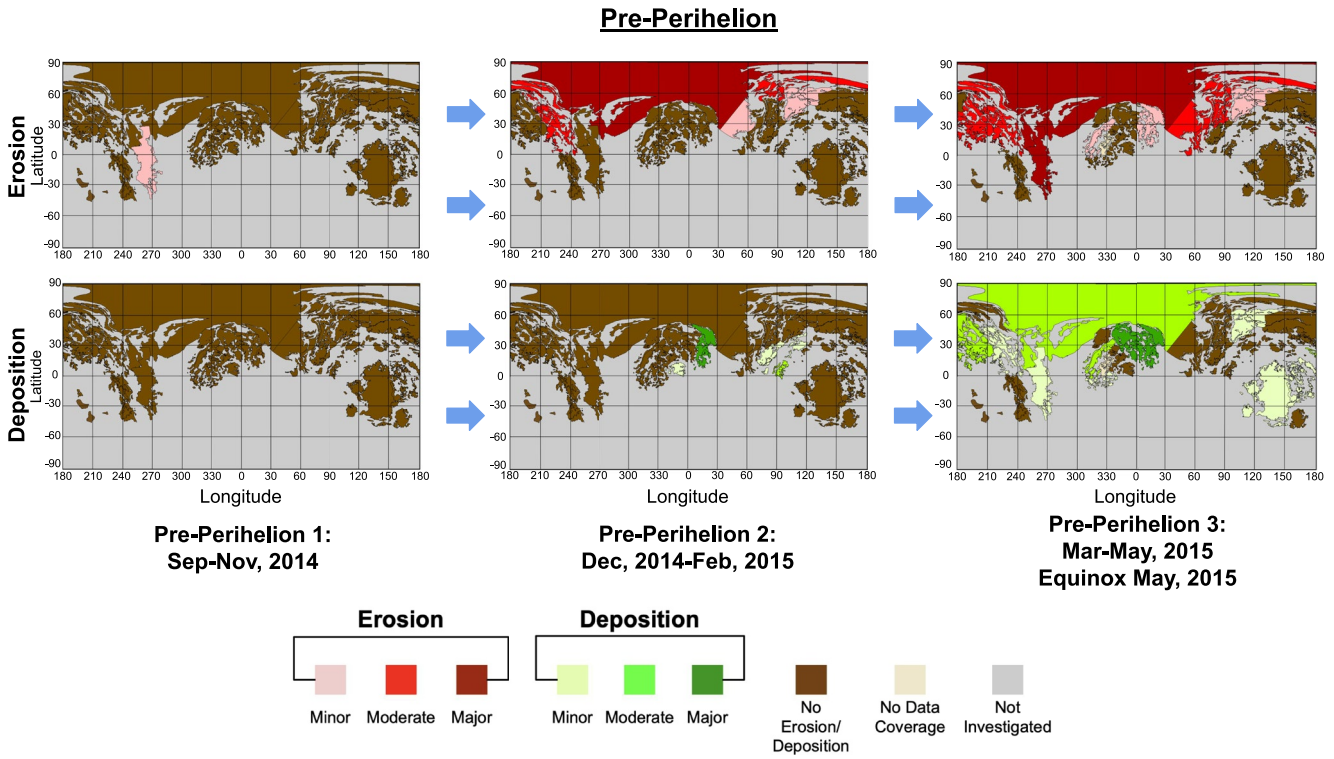

Figure 7. Equirectangular projections of smooth terrain activity in 67P organized to show the progression of erosion (top) and deposition (bottom) across three pre-perihelion time bins. Each column represents one time bin. Maps on the top/bottom indicate the intensity of erosion/deposition. Erosion began in the neck, then also activated in the internal regions of the large lobe, followed by lower latitudes on both lobes. Larger scale deposition occurred during Pre-perihelion 3 in many of the same regions experiencing erosion, with additional deposition occurring on top of the small lobe in Ma'at 2–4.

we still used scarp fading/burial to better interpret trends in our data when appropriate. Finally, the reformation of ripples in Hapi 1, as well as the general migration of plains, are classified as redistributions of sediment. We specifically classify these separately because though we know changes occurred, we cannot conclude whether net erosion or deposition occurred (or if it was net zero) due to the lack of nearby topographic benchmarks such as boulders or the underlying nucleus. For example, the migration of plains materials and dune-like crests clearly show the movement of granular materials, but the movement could be due either to small impacts splashing particles on the surface downslope (N. Thomas et al., 2015b) or due to ice sublimation in the near surface moving small volumes of materials, neither of which results in a clear topographic change of the granular surface layer.

3. Results

3.1. Pre-Perihelion Activity

3.1.1. Pre-Perihelion 1 (September–November 2014)

During this period, we observed erosion to be the earliest sign of surface activity on 67P. We did not observe any evidence of deposition during this time frame. This activity was limited to Hapi 1, located in the neck of 67P, although Barucci et al. (2016) observed limited erosion on the large lobe.

3.1.1.1. Large Lobe

Barucci et al. (2016) first described the presence of bright patches during this epoch, the spectral brightness of which they attributed to the presence of water ice. These patches occurred as individual boulders/patches in a western alcove of Imhotep 1 and in Imhotep 1's eastern pitted region (Barucci et al., 2016), and as a cluster at the boundary of Imhotep 1 and Apis (Barucci et al., 2016; Oklay et al., 2016). These specific features persisted for months, although lifespans of other bright spots varied (Barucci et al., 2016). We did not search for instances of bright patches in this work as they often occurred at consolidated borders between smooth terrain regions. We detected no erosional activity in smooth terrains associated with these spectral changes.

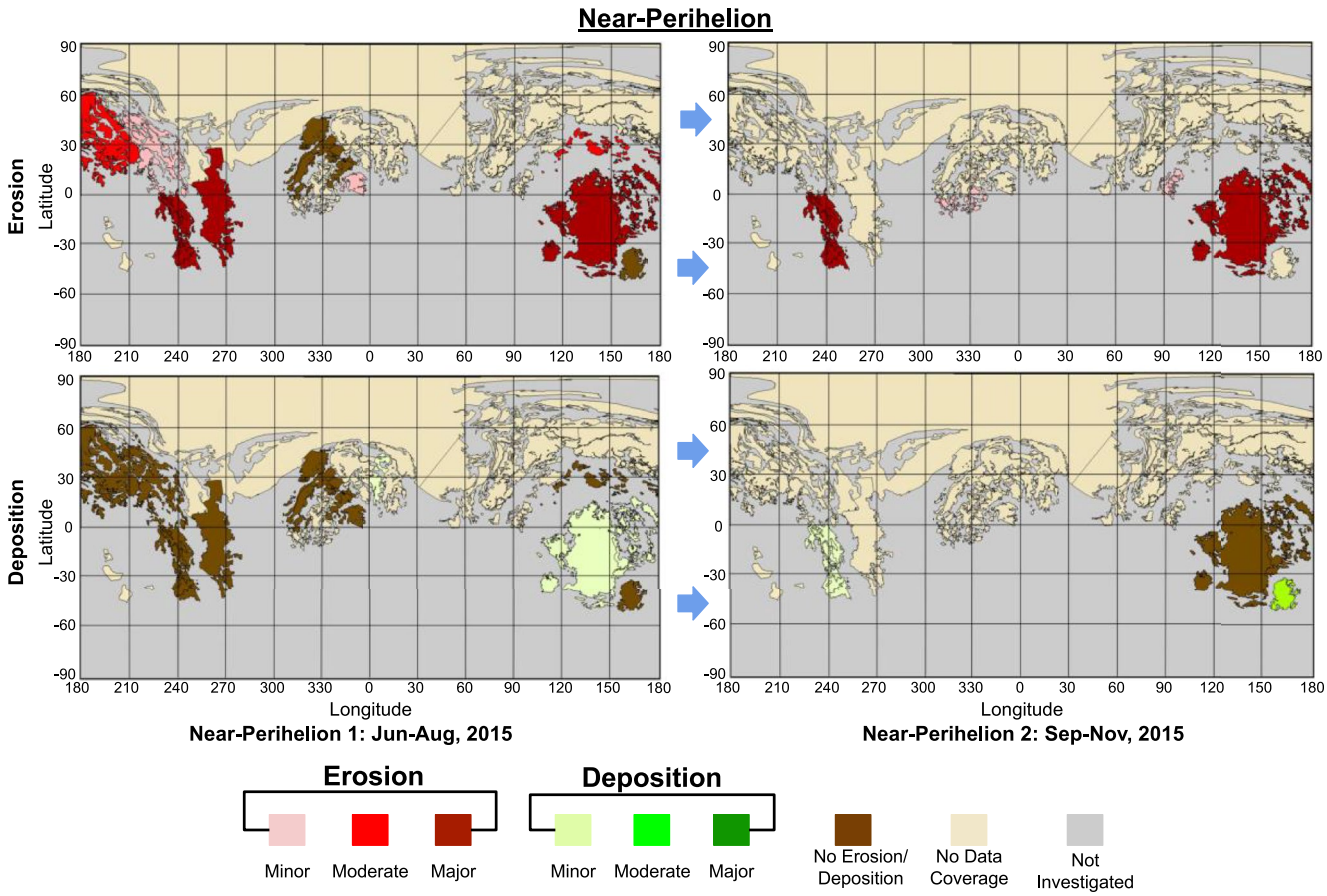

Figure 8. Equirectangular projections of smooth terrain activity in 67P organized to show the progression of erosion (top) and deposition (bottom) across two time bins near 67P's perihelion on 13 August 2015. As a result of decreased image resolution, tan-colored regions were not observable, leaving only the more external regions of the lobe for observation. We observed erosion centered around the mid to low latitudes over these time bins, with some of the eroded material appearing to locally re-distribute. Material from Anubis' scarp migrations appears to fall back into the same region, while sediment lofted from Imhotep 1 appears to deposit both within the same region, and in the nearby alcove of Imhotep 2.

3.1.1.2. Small Lobe

We observed no activity on the small lobe during this period.

3.1.1.3. Neck

We first observed erosion on 67P within Hapi 1, where two boulders were exposed in the center of the region on 12 September 2014. We also observed the potential migration of features analogous to aeolian ripples (Davidsson et al., 2021; El-Maarry et al., 2017, 2019; Jia et al., 2017) in Hapi 1 from 2 September–12 September 2014, although such changes may also be artifacts of the image projection process. As a result, we did not include them in our interpretations.

3.1.2. Pre-Perihelion 2 (December 2014–February 2015)

Erosion, deposition and redistribution of smooth terrains began in earnest during Pre-Perihelion 2 (Figure 7). With the exception of Ash 3, we consider all of these regions where we observe erosion to be "internal," meaning they are all located directly within or near the neck and have a significant portion of their surface tilted toward the Hathor cliff. While many of these regions are proximal to the neck, our observations clearly show that erosional activity also expanded south of (away from) the neck.

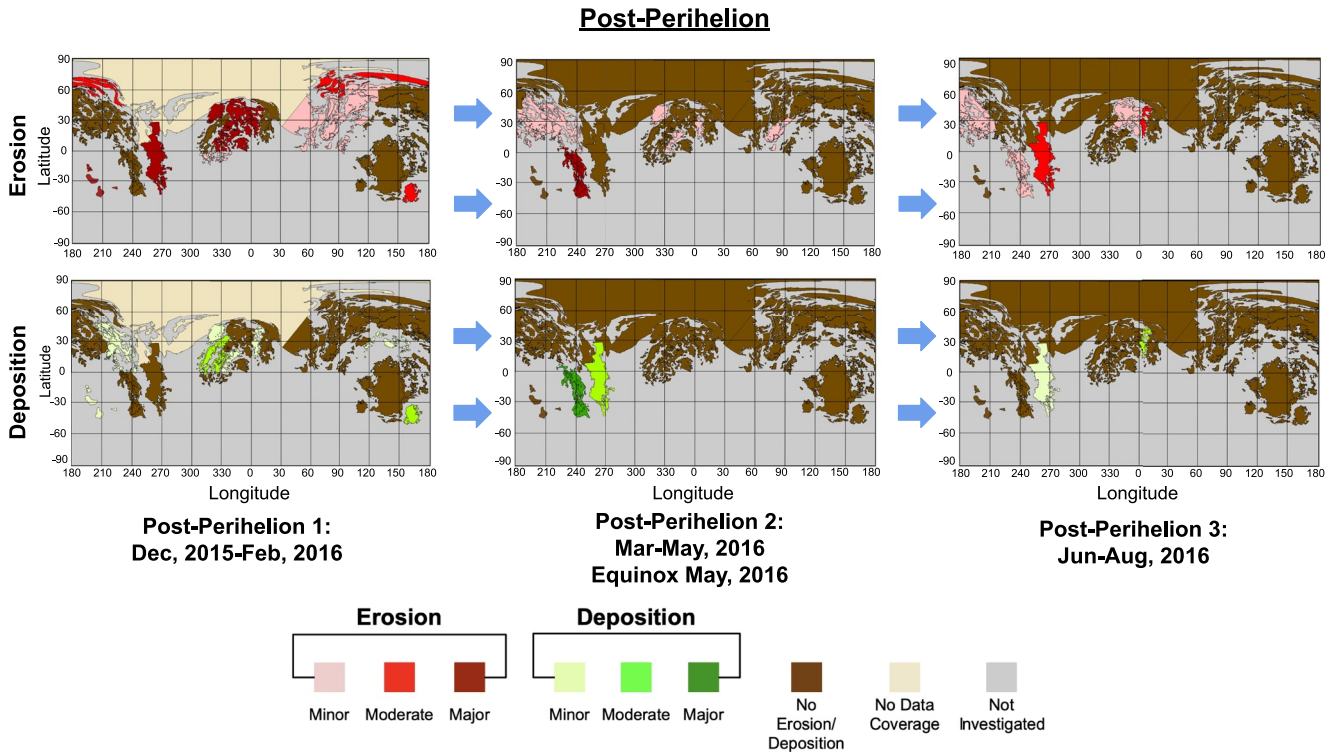

Figure 9. Equirectangular projections of smooth terrain activity in 67P organized to show the progression of erosion (top) and deposition (bottom) over three time bins occurring after 67P's perihelion passage. As Rosetta returned to lower altitudes, image resolution improved, revealing the majority of the comet surface for observation by March 2016. Much of the erosion and deposition we observed in the northern hemisphere may have occurred closer to perihelion, as a result of the data limitations shown in Figure 8. Lower levels of both erosion and deposition continued throughout the remainder of the mission, with spatial trends in the locations of where material was lofted and re-deposited.

3.1.2.1. Large Lobe

We detected scarps migrating within Seth 2 by December 2014 and within Seth 1 by 23 January 2014. These scarp migrations continued through February 2015 in both regions. We also observed two boulder exposures in Ash 3 by 2 December 2014.

We discovered the first clear evidence of deposition of new smooth terrain materials in Babi 2, Aten 1, and Aten 2 (Figure 7) in February of 2015, regions which are generally located south of the initial erosion activity dominated by Hapi 2 and Hapi 3, described below. We identified isolated instances of boulder and nucleus burials within Babi 2 on 19 February 2015.

3.1.2.2. Small Lobe

Hu et al. (2017) and El-Maarry et al. (2019) described honeycombs that began to display an increase in roughness in Ma'at by 22 January 2015, and in the Nut and Serqet regions by 14 February 2015. These include depressions that would later mature into honeycombs. However, we did not detect these changes, or any other erosional activity.

On the small lobe, we observed deposition in Hatmehit, and Ma'at 4 (Figure 7) in February of 2015. As with the deposition we observed on the large lobe, these regions are located south of erosion activity in this period. We identified both boulder and nucleus burials within Hatmehit on 20 February 2015. Across the entire nucleus, the most significant and obvious deposition in this time period occurred in Ma'at 4. In this region, the newly deposited material covered at least 11 large boulders and numerous nucleus outcrops that span the width of the entire sub-region by 21 February 2015. This early deposition marked the beginning of a widespread deposition event which continued in Ma'at 4 and in neighboring regions of Ma'at for several months. Notably, this depositional event over a significant portion of the small lobe coincided precisely with erosional activity in the Hapi 2 region. Hapi 2 is proximal to Ma'at 3 and 4, lying just to the north in the deep gravitational low of the neck. This may

indicate a causal relationship, described in Section 4.1. We observed the large-scale redistribution of smooth terrain materials within the nearby region of Ma'at 4 on 21 February 2015.

3.1.2.3. Neck

We detected scarps migrating within Hapi 2 and Hapi 3 during this period. The migrating scarps within Hapi 2 are of particular interest, as large quasi-arcuate scarp fronts emanated from 67P's north pole toward Hapi 1 and Hapi 3 between 30 December 2014 and 9 February 2015. While scarp migrations were recorded in the Hapi region by El-Maarry et al. (2017), we show here that they began at least 1 month prior to their observations. These scarp migrations continued in both Hapi 2 and Hapi 3 through February 2015. We also observed boulder exposures in Hapi 3, and possibly in Hapi 2. Much greater erosion appears to have occurred within Hapi 2 as migrating scarps exposed five boulders on 30 December 2014, and another 16 by 22 January 2015.

3.1.3. Pre-Perihelion 3 (March–May 2015)

During this period, the magnitude of erosional and depositional activity strongly increased, and the spatial coverage of this activity continued to expand southward as 67P approached equinox in March 2015. We detected at least 56 instances of boulder or nucleus burials during this period. In several instances, erosion and deposition appeared to be occurring simultaneously. This pattern suggests that either (a) local sediment fallback from smooth terrain erosion was working in tandem with the generation of new sediment in the southern hemisphere to reshape the north, and/or (b) transport distances of sediment within smooth terrains occurred over short, sub-kilometer distances.

3.1.3.1. Large Lobe

Erosion expanded into the low and mid-latitudinal regions of Ash 1, and Babi 1 during Pre-Perihelion 3. We observed numerous migrating scarps within a highly localized, low latitude area of Ash 1 on 22 April and 16 May 2015. Each scarp appeared to expand radially in an eastward direction and emanated from the base of a local cliff. We detected polygonal scarps migrating within Babi 1, an internal sub-region of Babi (Figure 1), from 14 March–10 May 2015. We first saw scarps appear on terraces proximal to the neck in March, followed by the expansion of these scarps and the formation of a new polygonal scarp in a northern terrace of the region by 19 April 2015. We also identified a scarp expanding in the southernmost active terrace of Babi 1 by 10 May 2015. Scarp migration continued in Seth 1 and Seth 2, observed on 5 March 2015 and April 2015, coinciding with the redistribution of sediment in these regions. We also observed three boulder exposures within Seth 1 on 25 April 2015, as well as sediment slumping in Ash 1 by 16 May 2015, although this change may have been gravitationally influenced.

Honeycombs matured within Seth 1 (increased in surface roughness) by 25 April 2015. Hu et al. (2017) also recorded honeycombs evolving in Babi 2 by late March 2015. Barucci et al. (2016) and Deshapriya et al. (2016) described the evolution of one bright patch in Khonsu, which persisted from 10 March to 22 May 2015. We identified various combinations of nucleus and boulder burials in Ash 1, Ash 3, by April 2015, and within Seth 1 and Imhotep 1 by May 2015 indicating depositional activity.

3.1.3.2. Small Lobe

In Pre-Perihelion 3, erosion expanded across the small lobe into Ma'at 4. Nearby, Hu et al. (2017) recorded two small scarps migrating in Ma'at 3 by 28 March 2015 which exposed part of the underlying nucleus. Additionally, we observed the exposure of the underlying nucleus in Ma'at 4 by 16 May 2015. Honeycombs within Serqet and Ma'at 3 also matured during this period, on 5 March, 28 March 2015, respectively. El-Maarry et al. (2017, 2019) and Hu et al. (2017) identified maturing honeycombs in Serqet, near our own observations in Ma'at 3, and consistent with observations of Shi et al. (2016).

We identified nucleus and boulder burials in Serqet and Maftet by 5 March 2015 and Ma'at 4 by April 2015, and within Serqet, Ma'at 2, Ma'at 3, and Ma'at 4 by May 2015. We also identified the burial of a small circular depression in Serqet (10 May 2015) during this period. This pattern mirrors the activity observed on the large lobe.

3.1.3.3. Neck

We observed the continued migration of 10–100 m wide scarps within Hapi 1, 2, and 3 throughout March–May (Birch et al., 2019; El-Maarry et al., 2017, 2019), as many more irregular scarp fronts formed within these three regions. Although Birch et al. (2019) recorded the last day of scarp migration in Hapi 1 to be 22 April 2015, we detected activity up to 1 month later on 23 May 2015. During this sequence of scarp activity within the neck,

we observed the destruction of the ripple formation in Hapi 1 by radially expanding scarps. These scarps first traveled through the region on 25 April 2015, consistent with the observations of El-Maarry et al. (2017, 2019). We found further evidence of erosion by the exposures of four boulders within Hapi 1 on 25 April 2015. We also recorded multiple instances of nucleus and boulder burials in Hapi 1 and Hapi 2 by April 2015.

3.2. Near-Perihelion Activity

3.2.1. Near-Perihelion 1 (June–August 2015)

As the comet approached perihelion, significant gaps in data coverage arose due to Rosetta's large distance from 67P. During Near-Perihelion 1 (June–August 2015), primarily only low latitudinal external (i.e., non-neck or Hathor-facing) regions were analyzed. Hapi 1 and Seth 1 were the only internal regions with favorable viewing conditions at this time. Barucci et al. (2016) also noted that bright patch production peaked during this epoch, approximately at perihelion, lending credence to their erosional origins.

We searched for and located many evolving honeycomb features throughout the mission; however, our image processing sometimes limited our ability to clearly discern such detailed changes in surface expression. In the case of the depressions on the Ash/Seth border, as well as honeycombs in Serqet, this led to a later detection date in our data set (∼1 month). However, we did often detect the large-scale migrations of plains and crests within smooth terrains, as described above within Ma'at 4, and which we also identified in Seth 1 (23 January 2015), Seth 2 (12 December 2014), and Hapi 1 (14 February 2015).

3.2.1.1. Large Lobe

One isolated scarp formed in Seth 1, on 17 June 2015, but no other activity was visible in the region in this period. We detected varying degrees of erosion in the external regions Ash 4, Anubis, and Imhotep 1. The most notable activity in Near-Perihelion 1 occurred in Imhotep 1, which includes the primary basin on the large lobe, as well as the western and southwestern alcoves. Within the primary basin and the western alcove, we observed numerous scarp fronts migrating tens to hundreds of meters over the duration of the epoch, specifically on June 5, June 27, July 11, July 26, August 1, August 9, and 23 August 2015, consistent with the observations of Groussin et al. (2015) through July 2015. Jindal et al. (2022) recorded the onset of scarp migrations in Imhotep 1 2 days prior to our observations, on 3 June, and measured an average rate of migration between 3 June and 27 June to be ∼23 cm/hr, with migration rates varying between scarps. As the comet drew closer to perihelion (13 August 2015), scarp activity trended southward, following the subsolar latitude (Figure 6; Jindal et al., 2022). This included the formation of a curvilinear scarp in the southwestern alcove of Imhotep 1 on 26 July 2015, which migrated further south on 1 August 2015. This activity marked the onset of scarp formations and migrations that expanded across the entire Imhotep 1 basin for a brief but extremely active six month period. Barucci et al. (2016) also recorded the presence of a short-lived bright patch on the eastern periphery of Imhotep 1, coinciding precisely with the onset of the region's scarp activity. The patch persisted from 5–27 June 2015, waning from a diameter of 57–36 m. We identified a scarp front expanding within a large pre-existing scarp in Anubis' northern region from 11 July–1 August 2015, and a boulder migrating within an area of coarser sediment farther north on 26 July 2015. We detected two scarps which formed in Ash 4, located north of Imhotep 1 on the face of the large lobe, on 13 June and 18 July 2015, emanating from a western cliff at the edge of the basin. The scarps then migrated eastward and merged on 9 August 2015. Another notable erosional event during this period occurred in Seth 2. A cliff previously referred to as "Aswan" (Pajola et al., 2016) collapsed at the edge of Seth 2's large, flat terrace (El-Maarry et al., 2019; Pajola et al., 2017). The collapse was first identified on 15 July 2015. While the cliff collapse involved initially consolidated materials, it created talus deposits which landed on a sediment-covered plateau at a lower elevation, within Hapi 2. Pajola et al. (2017) measured boulders ≥1.5 m before and after the cliff collapse to have increased from ∼12,000 to ∼18,000.

The only observable deposition that occurred in this time period was detected in Imhotep 1. A meter-scale boulder was buried within the primary Imhotep basin on 26 July 2015. While we did not use the burial of scarps to detect deposition, Jindal et al. (2022) detected the burial of one scarp on 11 July 2015, three scarps on 26 July 2015, a pit on 31 July 2015 and one final scarp on 6 August 2015, indicating that deposition was still occurring during the peak of 67P's erosional activity. This conclusion is particularly supported by images from the weeks after perihelion (23 August–4 September 2015), as actively migrating scarps were buried by fresh deposition (Jindal et al., 2022). This likely indicates a point at which net local deposition outpaced local erosion in the

Imhotep 1 basin. Some of these freshly deposited smooth terrains may also represent grains that could not escape 67P after being ejected by nearby scarp migration activity. We observed plain migrations on top of the large lobe during this period, within Ash 1(1 July 2015), and Ash 4 (18 July, 9 August 2015).

3.2.1.2. Small Lobe

On the small lobe, we only detected isolated evidence of erosion, as one boulder migrated ∼10 m in Hatmehit by 7 July 2015. We observed a migrating patch of plains in the western area of this region from 27 June–7 July 2015. We identified plains migrating in several other regions across the northern hemisphere, including Serqet (25 June, 4 July 2015), and Maftet (11 July 2015) on the small lobe. The plains migrating in Maftet substantially affected the distribution of its smooth materials well into Pre-Perihelion 2, though we lack the high-resolution data necessary to precisely determine the end date of this surface activity. On 11 July 2015, one honeycomb feature located among Maftet's migrating plains began to change shape slightly as the smooth terrains were locally redistributed, although it is unclear if the feature's surface roughness visibly changed on this date.

3.2.1.3. Neck

Scarps continued to migrate in Hapi 1 during this period. A ∼250 m wide scarp progressed away from the rotation axis (southward), and a scarp shaped like a shepherd's crook unfurled and expanded through the initial location of the aeolian ripples on 27 June 2015. These two scarp fronts later merged on 19 July 2015. We detected the aeolian ripples re-forming at least two distinct crests inside the curved shepherd's crook-shaped scarp of Hapi 1, on 11 July 2015 (Figure S1 in Supporting Information S1), several months prior to observations by El-Maarry et al. (2017, 2019). One week after the initial ripple reformation, a third visible crest formed inside the shepherd's crook-shaped scarp, although the crest positions did not reach their final location until the next period. This suggests that these crests (or the intervening relative "anti-crests") have a preference for this location on 67P. Plains migrated in Hapi 1 during the same time interval as the continuing scarp activity (11 July, 25 July 2015).

3.2.2. Near-Perihelion 2 (September–November 2015)

Resolution decreases further during Near-Perihelion 2 (September–November 2015), with only about half of the regions sufficiently imaged for our analysis. Even with such limited information, we see extensive changes to 67P's smooth terrains.

3.2.2.1. Large Lobe

Scarps continued to migrate within Imhotep 1, first continuing their migration only in the southern portion of the region on 2 September 2015, then restarting again in the northern hemisphere on 26 October and 21 November 2018. A ∼100 m scale scarp migrated south between 2 September and 21 November 2015, exposing a meter scale boulder in the process. We observed no further scarp migration in Imhotep 1 after 28 November 2015 (Movie S1), although Jindal et al. (2022) documented the migration of one final scarp in December 2015. We did identify a migration of the northern pre-existing scarp front in Anubis on 15 September 2015. By 28 November 2015 both the northern and southern hemispheric scarp fronts remaining in Anubis from 67P's previous perihelion approach migrated. These two scarp migrations were described by El-Maarry et al. (2017, 2019), although they first detected these changes in June 2016. Several smaller scarp fronts within and around these two larger features also migrated by 28 November 2015, indicating widespread erosion across the region. These observations are all coincident with the location of the subsolar latitude (Figure 6). We identified additional evidence of erosion in Aten 1, where four boulders migrated by 28 November 2015.

We observed one boulder burial in Imhotep 2 by 21 November 2015, and one boulder burial within Anubis by 28 November 2015. We found no further evidence of deposition during this period, however Jindal et al. (2022) did observe local deposition in Imhotep 1 by tracking disappearing scarp fronts, noting an interesting change in activity during the weeks following perihelion. They tracked the partial and complete burial of six scarps, even as some scarps continued to migrate. This suggests that while deposition and erosion were happening in Imhotep 1 simultaneously, the rate of local deposition across the primary basin began to overcome the rate of local erosion around 29 November 2015 (Jindal et al., 2022).

We also discovered plains migrating within Anubis (15 September 2015) and Imhotep 2 (21 November 2015). Interestingly, in Anubis, the freshly liberated sediment from the erosion described above appears to have

redistributed within the same region, causing the boulder burial observed on 28 November 2015, described above. Similarly, material lofted from within Imhotep 1 appears to have landed southeast in Imhotep 2, causing the boulder burial observed on 21 November 2015.

3.2.2.2. Small Lobe

We identified additional evidence of erosion in Maftet, with sediment continuing to redistribute, exposing one boulder and causing two others to migrate. In this region, local redistribution began in July 2015, with new crest positions observable as late as February 2016. During this redistribution process, a ∼50 m long pit formed by 23 November 2015. We also observed plains migrating within Hatmehit (7 November 2015) and Ma'at 4 (12 November 2015). The most drastic of plain migrations occurred in Imhotep 2 (see discussion above) and Maftet, although our resolution limits us from observing whether the plains within Maftet evolved as rapidly or over longer periods as Imhotep 2.

3.2.2.3. Neck

We did not observe any activity in the neck at this time due to imaging constraints.

3.3. Post-Perihelion Activity

3.3.1. Post-Perihelion 1 (December 2015–February 2016)

By Post-Perihelion 1 (December 2015–February 2016), Rosetta returned to its lower altitude orbits, which improved resolution sufficiently to view much of the comet surface in detail once again and observe any changes that took place throughout perihelion.

3.3.1.1. Large Lobe

We only observed evidence of erosion in isolated regions on the large lobe during Post-Perihelion 1. The dynamic activity of Imhotep 1 occurring closer to perihelion did not persist. We observed the exposure of circular pits from beneath a sedimentary cover in the eastern region of Imhotep 1 by February 2016, consistent with El-Maarry et al. (2017, 2019). The most significant erosional changes on the large lobe occurred within Khonsu, located southeast of Imhotep 1 (Figure 1). Activity within Khonsu began by 18 December 2015, where a boulder ∼40 m in diameter migrated ∼170 m northward, carving a scar into the nucleus (El-Maarry et al., 2017). Vincent et al. (2016) describe two possible outbursts which may have triggered the downslope rolling of this massive boulder on 1 August 2015 (Near-Perihelion 1), and on 14 September 2015 (Near-Perihelion 2), indicating that the boulder could have migrated earlier than either El-Maarry et al. (2017) or our own observations suggest. Four scarps also migrated in a patch of smooth terrains located in the northern portion of Khonsu, exposing three boulders along their paths on 18 December 2015. One boulder in the same area and a second boulder located in the center of Khonsu also migrated on this date. Four more boulders migrated across the region, and another five boulders were exposed by migrating plains by 23 January 2016.

Three bright pits formed in a central region of Khonsu's smooth terrains on the same date (Figure 5). The pits appear to have been pre-existing sediment-mantled structures that were further excavated. Previous analyses suggested that the fresh layer revealed in this process was rich in both water ice and other refractory materials (Deshapriya et al., 2016; Fornasier et al., 2015), showing spectral similarities to other erosionally active smooth terrains (Deshapriya et al., 2016; Oklay et al., 2016). The pits waned in overall brightness and area over the rest of the mission; however, some excess brightness was still detected on 30 July 2016 (Post-Perihelion 3), the last day the they were imaged by Rosetta. It is possible that these pits are analogous to bright spots described by Barucci et al. (2016) and Deshapriya et al. (2016). Deshapriya et al. (2016) described two such bright spots in the Khonsu region. The first (bright spot 2) is located on a "boomerang" shaped feature, and persisted from 23 January to 24 June 2016, while the second (bright spot 3) likely had a much shorter lifetime, as it was only observed once on 10 February 2016. Deshapriya et al. (2016) also correlated the presence of bright spot 2 with an outburst which occurred on 1 August 2015 (Vincent et al., 2016), which may indicate that it persisted for almost 1 year. Similar to the bright pits, Deshapriya et al. (2016) found that the spectra of the bright spots indicated that they were enriched in water ice.

To the northwest, eight boulders were exposed by migrating smooth terrains in Imhotep 2 on 23 January 2016, after which we saw no further activity in the region. We detected boulder migrations in Aten 1 on 2 December

2015, and in both Aten 1 and 2 on 17 January 2016, after which no further changes in either region occurred. We identified widespread erosional activity southeast of Aten 2, in Ash 4, as six boulders across the region were exposed and one migrated by 26 December 2015. However, only one isolated boulder was exposed in Ash 3, north of Aten 2, by 2 December 2015. Similarly, we located one boulder exposure in Babi 2, the external section of Babi west of Aten 1, on 26 December 2015, and the evolution of a pit field in a southeastern alcove of the region by 27 February 2016. We also identified limited erosion within Babi's internal section, Babi 1, although this is one of the few regions in which scarp migrations were still taking place. In Seth 1, another internal region, we detected two boulder migrations. We found slightly more activity in Seth 2, as the boundaries of scarps bordering the primary terrace migrated and new talus was deposited in two terraces on 17 January 2016.

We detected two boulder burials in a western strip of Ash 4's smooth terrains on 2 December 2015. Newly deposited material buried an exposed cliff on the western rim of Imhotep 2 on 23 January 2016, the same area in which a neighboring boulder was buried during the previous period. We observed one boulder burial within Khonsu on 23 January 2016, which may be linked to the formation of the spectrally bright pits nearby. We also observed evidence of deposition as evolving honeycomb structures decreased in visible surface roughness in Seth 1 by 17 January 2016.

We observed migrating smooth terrains in Ash 4 (2 December, 26 December 2015), Khonsu (18 December, 31 December 2015, and 23 January 2016), Imhotep 2 (23 January 2016), and possibly Babi 2 (2 December 2015).

3.3.1.2. Small Lobe

The most evident erosion detected during this period occurred on the small lobes, particularly in Ma'at 1, Ma'at 2, and Ma'at 3 from December 2015 to February 2016. In addition, we observed several boulder migrations and the formation of quasi-circular, ∼5 m diameter pits in Ma'at 2 on 17 January and 27 February 2016. We do not interpret these pits to be scarps because they did not migrate or expand after their initial formation. Similar features formed within Ash 1 during Post-Perihelion 2 (described below). Significant erosion also occurred in regions neighboring Ma'at during this period. We detected three boulder exposures and three boulder migrations west of Ma'at 1, in Nut by 20 December 2015. As resolution improved, we observed two more boulder migrations and 22 boulder exposures, generally in the northern half of the region, in Nut on 27 February 2016. Further to the west, in Maftet, the only direct evidence of local erosion came from one boulder migration, which we detected on 23 January 2016. On the face of the small lobe, we identified only limited scarp activity within Hatmehit, where one linear scarp and one curvilinear scarp both expanded southward on 17 December 2015. Five boulders were also exposed across the western half of the region by 27 February 2016.

We identified two boulder burials in Ma'at 1 on the same date, three more within Ma'at 3 by 17 January 2016, and four boulder burials in Nut by 27 February 2016. We also observed evidence of deposition in several of these regions by their evolving honeycomb structures, which decreased in visible surface roughness. These changes occurred within Ma'at 3 and Serqet by 17 January 2016.

We observed migrating plains in Ma'at 1 (2 December 2015), Nut (20 December 2015, 27 February 2016), Ma'at 2 (17 January, 27 February 2016), Ma'at 3 (17 January, 27 February 2016),Maftet (10 February 2016), and Hatmehit (27 February 2016).

3.3.1.3. Neck

In the neck, Hapi 2 was in polar winter, and was infrequently imaged over this period of time, preventing our search for surface changes. We did, however, observe active erosion in Hapi 1 and Hapi 3. Seven boulders were exposed, and one boulder migrated within a consolidated area on the eastern periphery of Hapi 1, on 2 December 2015. We detected two more boulder exposures in Hapi 1 on 9 January 2016 with improved image resolution. One week later, we identified one scarp migration, and two small boulder exposures in Hapi 3.

Similar to observations by Jindal et al. (2022), El-Maarry et al. (2017, 2019) described scarp fronts which previously destroyed Hapi 1's ripple formation had faded by December 2015. Based on this evidence and our own observations of newly deposited material in neighboring regions, we interpreted this fading scarp to indicate local deposition.

3.3.2. Post-Perihelion 2 (March–May 2016)

During Post-Perihelion 2, we observed an increase in erosion in the equatorial latitudes of the northern hemisphere as the subsolar point migrated north, across the equator.

While we detect no further evidence of sublimation-driven erosion, Deshapriya et al. (2016) documented the formation of a cluster of bright boulders (bright spot 4) on 7 May 2016, which persisted for 6 weeks after their nominal detection.

3.3.2.1. Large Lobe

On the large lobe, the most significant erosion occurred during this time in Anubis. While we found two boulder migrations and 41 boulder exposures spanning the length of the region on 10 April 2016, uncertainty in their occurrence date due to resolution limitations indicates that activity could have been initiated as early as March 2015. It is likely that these boulder exposures were related to the migration of plains in the center of the Anubis region, which we observed on 15 September 2015, when the subsolar point would have been passing through the low latitudes of the southern hemisphere. Also on the large lobe, we detected the possible exposure of 7 boulders in Babi 2 on 13 March 2016, although this observation is questionable due to resolution limitations. We also observed the migration of surrounding plains and the exposure of an outcrop of consolidated nucleus in Babi 2 on 13 April 2016, which had been buried by sediment on 19 February 2015. While we only located one boulder migration in Seth 1 on 28 April 2016, we saw a less frequent activity in Ash 1. In this region, we detected one boulder exposure and the formation of seven quasi-circular pits on 30 April 2016, similar to those that formed within Ma'at 2 during the previous epoch. We identified two new pits forming, although in a different location, within Ash 1 on 9 May 2015. As seen in Ma'at 2, we did not observe these pits growing or migrating after their initial formation; therefore, we do not classify them as scarp activity, although they appear to be the result of erosional activity.

As described for several other regions above, we observed that simultaneous deposition and erosion occurred in Anubis during Post-Perihelion 2. Twelve boulders were buried in Anubis by 10 April 2016, primarily within the same region where migrating plains exposed boulders. We observed local redistribution of materials in Anubis over Pre-Perihelion 2, with much of the redistributed material possibly sourced from the erosion within Anubis, which was exposed to direct solar insolation at the time.

3.3.2.2. Small Lobe

We first detected the exposure of three locations in Ma'at 3 on the small lobe, which may either be boulders or underlying nucleus. Two of these features had been buried during May 2015. We identified five boulder exposures in the southernmost portion of Ma'at 1 on 9 May 2016. El-Maarry et al. (2017, 2019) also recorded decreased surface roughness in honeycombs within Ma'at 3 during this period, although we did not identify this activity until 5 June 2016.

3.3.2.3. Neck

We detected deposition within the neighboring neck region of Hapi 1 that buried two m-scale boulders on 10 April 2016, perhaps suggesting that this infalling sediment may have also come from Anubis. El-Maarry et al. (2017, 2019) recorded the fading or partial burial of a scarp beneath the ripple formation in June, however we detected the fading of this scarp as early as 10 April 2016, coinciding with the burial of the two boulders described above.

3.3.3. Post-Perihelion 3 (June–August 2016)

During Post-Perihelion 3, at distances of >3 AU, scarp migration effectively ceased, as water ice transitioned from sublimative to radiative cooling, thereby drastically decreasing water ice activity. All evidence for local erosion and deposition decreased dramatically. While we did detect boulder exposures, migrations, and burials in several regions, these late observations may have been a result of increased resolution as Rosetta began to orbit closer to 67P's surface.

3.3.3.1. Large Lobe

An outburst was detected in Imhotep 2 on 3 July 2016 (El-Maarry et al., 2019; Vincent et al., 2016), although this event did not produce visible changes to nearby smooth terrains. We identified one sediment slump from smooth materials lying atop a cliff in the northern portion of Ash 3 on 5 June 2016. We observed five boulder exposures within Ash 1 by 6 June 2016, though data coverage and resolution limitations made it difficult to reliably determine when the exposures occurred. Likewise, we located a cluster of 5 boulder exposures in northern Anubis on 9 June 2016, which could have occurred as early as April 2016. While El-Maarry et al. (2017) showed that the two major pre-existing scarp fronts in Anubis migrated by June 2016, we show above that these migrations

occurred several months earlier, reaching their final positions on 28 November 2015 (Near Perihelion 2). Finally, in Khonsu, the visible brightness waned in the two largest ice-rich pits, although all three pits were still relatively bright compared to neighboring materials on 13 June 2016. This is the last evidence of erosion we detected in 67P's smooth terrains. Deshapriya et al. (2016) indicated that bright spot 2, also located in the Khonsu region, persisted as late as 24 June 2016.

3.3.3.2. Small Lobe

We identified two boulder exposures within a region of migrating plains in Ma'at 2, as well as three boulder exposures and one boulder migration in Ma'at 3 on 5 June 2016. New smooth deposits also buried three boulders within Ma'at 3 by 5 June 2016.

3.3.3.3. Neck

We detected 7 boulder exposures in Hapi 1 on 8 June 2016, although similar data limitations suggest that these exposures may have occurred in the previous period.

New smooth deposits buried one boulder within Hapi 1 by 8 June 2016. We observed no further evidence of deposition after this date.

As Rosetta began orbiting closer to 67P and eventually crash landed on its surface, images of complete to near complete regions of the comet were no longer available, preventing any further analysis of the comet's meter-to decameter scale surface changes.

4. Discussion

4.1. Key Takeaways

Based on the observations described above, we draw four main conclusions.

1. Sediment is intra- and inter-regionally transported.

While previous models suggest that sediment is first sourced by outgassing in the southern hemisphere (Keller et al., 2015), our observations suggest that significant volumes of sediment are also redistributed intra- and inter-regionally after their initial deposition. As the particles deposited within the smooth terrains are likely rich in water ice (Davidsson et al., 2021), we attribute this localized redistribution to post-emplacement sublimation of ice retained within the sediment itself. Evidence of this redistribution began as early as Pre-Perihelion 2, when the scarps migrating through Hapi 2 began to deposit sediment onto the low- and mid-latitudes of the small lobe, primarily in Ma'at 4 and Hatmehit. This process continued into Pre-Perihelion 3, as escalating scarp activity across Hapi 1, 2, and 3 jettisoned even more material, most of which appeared to deposit on top of the small lobe in regions Ma'at 2–4, and to a lesser extent, in Serqet and Maftet (Figure 7). Later, in Near-Perihelion 1, the energetic scarp-driven activity in the Imhotep 1 basin intra-regionally redistributed grains, burying a boulder, five scarps, and a pit in the process (Jindal et al., 2022). In Near-Perihelion 2, as scarp migrations continued in Imhotep 1, remobilized grains partially or completely buried six scarp fronts in Imhotep 1 and a consolidated cliff in Imhotep 2 (Figure 7).

Finally, in all Post-Perihelion phases, we observed the redistribution of grains from several sub-regions of Ma'at into Ma'at 3 (Post-Perihelion 1, 2, 3), simultaneous erosion and deposition activity in Khonsu (Post-Perihelion 1) and Anubis (Post-Perihelion 2), and the apparent transport of grains from Anubis to Hapi 1 (Post-Perihelion 2) (Figure 9).

However, a direct link between the possible sources and sinks of material cannot be definitively established. This is largely the result of the sporadic nature over which Rosetta OSIRIS NAC data were acquired, wherein we lack simultaneous observations of both a source and sink region, or any continuous/quasi-continuous imaging capable of resolving a given sediment transport pathway. Instead, we observe two regions eroding and depositing simultaneously and nearby each other (e.g., Hapi 2 and Ma'at 4 in March–May 2015) and infer that sediment is transporting between them. Our observations are therefore consistent, though perhaps not diagnostic, with some amount of intra- and inter-regional sediment redistribution, indicating possible sediment transport pathways by which smooth terrains can rearrange sediment locally over time.

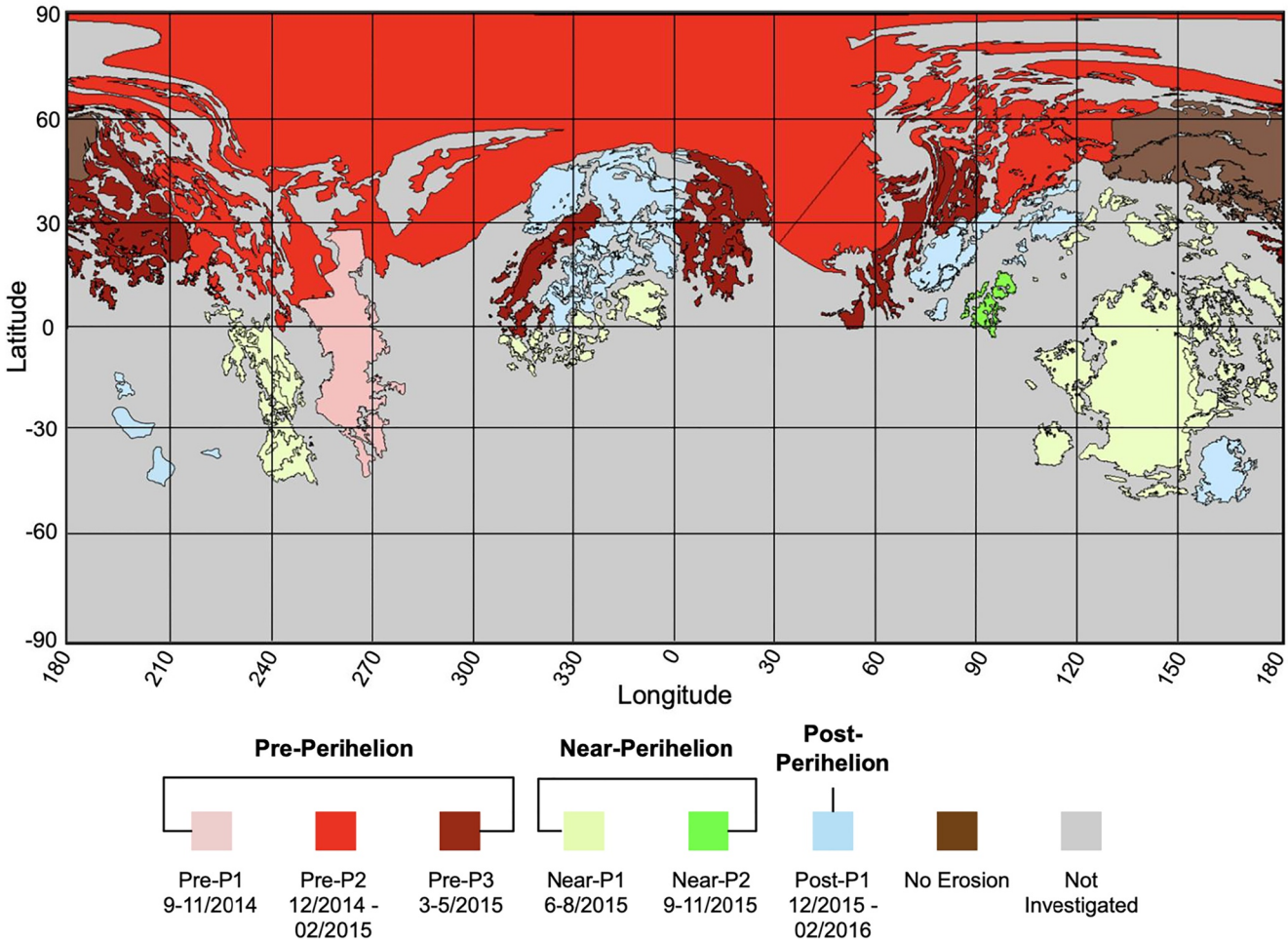

Figure 10. Equatorial projection showing the onset of local erosion by region, color coded to show pre-perihelion (shades of red), near-perihelion (shades of green), and post-perihelion (shades of blue) time bins. Regions in brown show zero evidence of erosion at any point during the period of our observations, while those in gray were not investigated due to a lack of observations or smooth terrains.

2. Erosion and deposition follow the subsolar latitude, and are strongly influenced by local topography.

Observable erosion began in the neck in Hapi 1, spread to the rest of the neck and internal/comet-facing regions, progressed "southward" onto the tops of the comet's lobes, further south onto the face of either lobe, and finally into the southern hemisphere near perihelion (Figures 7–10). The southward progression of erosional activity is consistent with the migration of the subsolar latitude as 67P approached perihelion (Figure 6; Keller & Kührt, 2020). Before perihelion, El-Maarry et al. (2019) and Hu et al. (2017) observed honeycomb maturation in the low- and mid-latitudes of Ma'at, Nut and Serqet south of our own observations of erosion. We interpret these honeycomb evolutions to be some of the earliest indicators of local erosion. We also observed evidence of local enhancement due to topographic self-heating in Hapi 2, where the cliffs of Hathor and Seth 2 re-radiated onto the neck, sustaining scarp migration events for over 6 months. Locations of enhanced activity in the neck and within isolated pits in other regions were modeled by Keller et al. (2015) and are consistent with observed activity in Hapi 2, as well as scarp activity observed in pits from the Ash 1 and Seth 1 regions.

Depositional activity followed a similar, although less direct trend, broadly beginning in regions near the neck and progressing southward, slightly lagging the subsolar latitude in time. Within any given region, we also observed heterogeneous deposition of new materials, suggesting that sediment transport pathways are often quite short. If we assume that the grains initially deposited as airfall are water ice-rich (Davidsson et al., 2021), then these local variations could result from two competing effects. First, a given location may have a limited supply of ice-rich sediment, wherein such regions are distant from a given source region and/or high relief topography

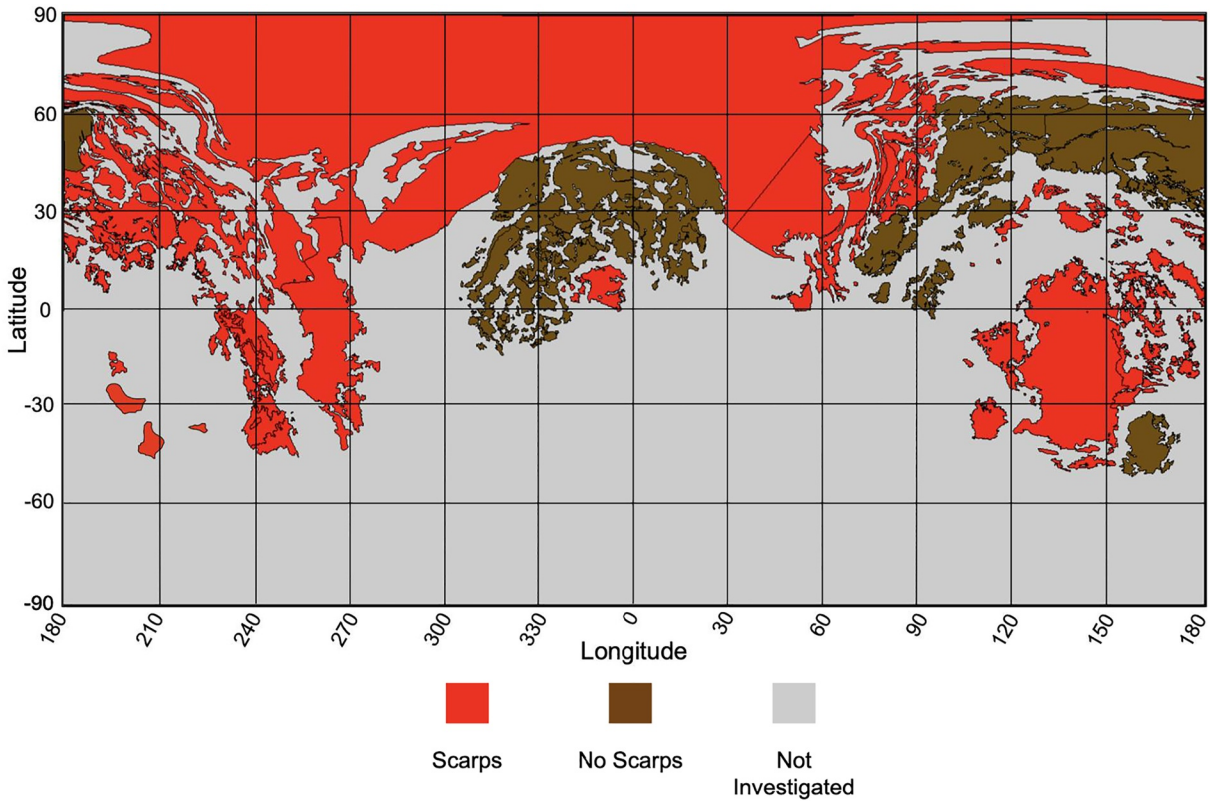

Figure 11. Equatorial projection documenting the distribution of scarp activity across 67P by region. Activity is focused in equatorial regions (~−30° to 30° latitude), and internal regions, which have increased energy input due to topographic self-heating. Although Ash 1 experienced scarp activity, all active areas of the region occur below 30° latitude.

block the delivery of new ice-rich particles—quantified via the "deliverability" index of Davidsson et al. (2021). Equally, sediment may either lack the necessary ice needed to re-mobilize sediment due to prolonged exposure during transport/on the surface, or sediment may be relaunched immediately upon deposition—quantified by the "survivability" described in Davidsson et al. (2021).

Topography can therefore both shield a location from receiving new material and also enhance the local erosion rates of any newly deposited material due to self-heating (Jindal et al., 2022). Thus, the large topographic variations across the comet may directly drive the observed highly localized nature of erosion and deposition. This pattern also suggests a remarkable terrestrial analog, wherein the topographic evolution of a given portion of 67P's smooth terrains is controlled by the capacity for sediment to be transported, and the supply over which it is delivered. Just as a river adjusts its geometry to varying sediment loads, so do 67P's smooth terrains.

3. Scarp activity is primarily limited to equatorial and internal regions.

As the primary driver of erosion in the smooth terrains (Birch et al., 2019), scarp activity is influenced both by the subsolar latitude and the presence of surrounding topography. On the external portions of the nucleus, topographic relief is lower, and the presence/absence of scarps follows the subsolar latitude (Figures 6 and 11). This trend was most apparent in Imhotep 1 during 67P's perihelion approach, where scarps began migrating in the northern portion of Imhotep 1 in June 2015. Progressively more southern scarps appeared and began migrating as the comet approached perihelion, consistent with observations by Jindal et al. (2022). By October 2015, we once again detected scarp migrations in the northern portion of the basin until all migration in Imhotep 1 stopped between November and December 2015. As a result of this insolation dependence (both direct and re-radiated from surrounding topography), scarp activity was primarily limited to low- to mid-latitudinal regions mostly bordering the equator (Khonsu, Anubis, Hatmehit, Imhotep 1, Ash 4) as 67P approached perihelion.

Meanwhile, on internal portions of the comet, the influence of topography becomes especially important. Specifically, any given spot of the surface on internal portions of 67P "sees" significant fractions of the comet above

their local horizon (Birch et al., 2019; Jindal et al., 2022). These surfaces then re-radiate onto the smooth terrain regions, providing a secondary heat source that is sufficient to form scarps. This was the case for Hapi 1, Hapi 2, Hapi 3, Seth 1, Seth 2, Babi 1, and Ash 1 (Figure 11). We also observed examples of re-radiation encouraging scarp formation in the neck and in pits containing smooth terrains in Ash 1 and Seth 1, and Imhotep 1 along several topographic boundaries that acted as discontinuities from which several scarps generated (Movie S1).

Other smooth terrains on 67P never showed evidence for scarps. In 67P's current orbital configuration, the mid- to high- latitudes (tops of either lobe) were in polar winter as the comet approached perihelion. The subsolar point passed through the lowest latitudes of these regions while the comet was still at distances of >2.5 AU from the Sun, providing much less total solar insolation to the tops of either lobe compared to the other external regions of the comet. Further, these regions lack significant topographic relief and the secondary energy source they provide.

Therefore, as in previous work, we suspect that scarp migration results from the complex interactions between 67P's high relief topography and the local, rapidly changing illumination conditions as 67P approached perihelion. This appears to produce highly localized enhancements in the total amount of energy a given location on the surface receives. Combined with the presence of local re-radiating hot spots such as boulders or cliffs within the plains (owing to being more conductive) (Marschall et al., 2017), scarp formation ends up being extremely localized, rather than a simple removal of an upper unconsolidated sedimentary layer (Birch et al., 2019; Jindal et al., 2022). This therefore explains why regions near 67P's north pole, which otherwise receive minimal direct illumination, can still host scarps, while for external regions, only those directly illuminated near perihelion 67P display scarps (Figure 11).

4. We observe net zero erosion/deposition on the tops of the lobes, perhaps indicating the presence of terminal sinks for airfalling sediment.

A final striking pattern we observe is that over 67P's mid-latitudes (30°N–60°N),which represent the “tops” of each lobe when viewed edge-on, the surface was largely inactive at Rosetta's NAC image resolution (Figure 12). Although deposition is inherently difficult to discern in the projected images, and the surface could have gained/lost sediment up to ∼50 cm depth without our detection (equal to the best resolution Rosetta obtained before/after perihelion), the absence of any activity stands in stark contrast to the rest of the comet. All other regions exhibited at least minor activity and reorganization of the overlying sedimentary cover, while these regions showed almost zero changes of any kind.

The clearest example is Ash 2, where we detected zero deposition or erosion activity of any kind. Also on the large lobe, we observed no activity from 40°N to 60°N in Ash 1, and the mid-latitudinal regions of Babi 1 and Seth 2 (Figure 12). We likewise identified very limited activity in Ash 3, most of which occurred as slumping of over-steepened mounds of smooth terrains along the margins of overhanging cliffs. While we detected isolated boulder exposures in this region, they were situated on relatively low elevation terraces within the elongated pit of the Aten region. In Ash 3 we likewise identified sediment that coated an outcrop of the underlying nucleus in April 2015, although the local burial appears to be the result of another gravitational slump of sediment.

We also observe limited surface activity from ∼40°N to 50°N latitude on the small lobe (Figure 12). Similar to Ash 2 and 3, these latitudes of the small lobe experienced polar night for a prolonged period near perihelion. Although boulders and outcrops of consolidated nucleus were exposed in Ma'at 1–4, this erosion all took place below ∼40°N, latitudes that never went into polar winter near perihelion. The remaining section of the top of the small lobe appeared unaltered by local erosion, except for one honeycomb evolution in Ma'at 1 that we interpret to be the result of self-heating from a nearby cliff. While we observed changing honeycomb maturity within the rest of Ma'at due to both erosion and deposition, these features were primarily located between 20°N and 40°N latitude (El-Maarry et al., 2019).

The lack of detectable activity in these regions is consistent with previous models. Keller et al. (2015) modeled erosion in these regions and their counterparts on the large lobe and estimated that they should be the least active locations on the comet. Keller et al. (2015) likewise noted that the most active sections of these regions were the sections that slope to the south, consistent with our observations of activity from 20°N to 40°N. Erosion and deposition models from Lai et al. (2016) also suggest that grains from about 0.04 to 0.08 mm in diameter should have deposited in these regions in January 2015, but grains from about 0.04 to 22 mm should have been eroding

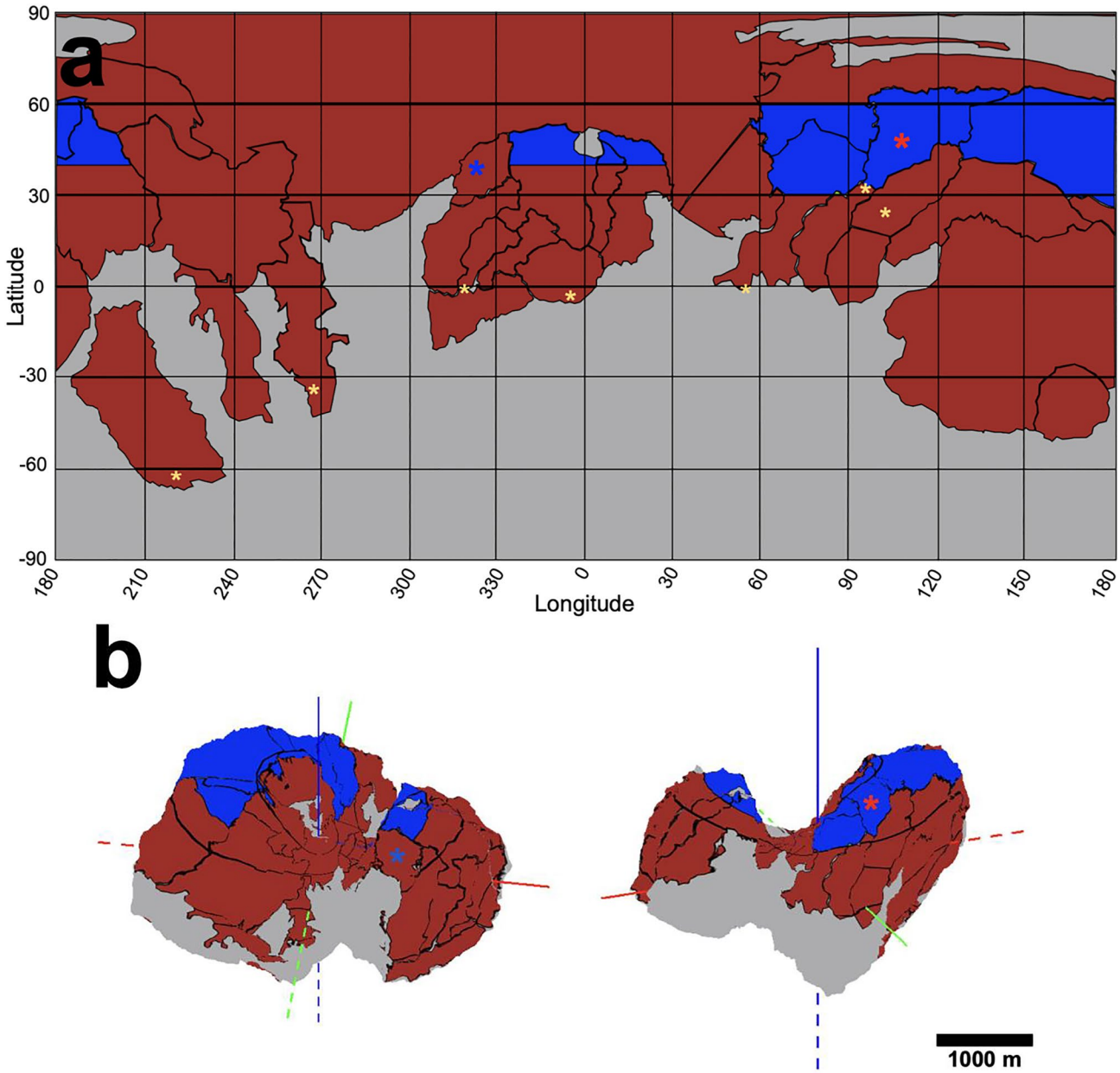

Figure 12. (a) Equirectangular projection showing latitudes with observed erosional or depositional activity (red), and regions with zero observed activity (blue). Regions are broken into latitude bins of ∼30°, except for subregions of Ma'at, which are broken into 10° latitude bins to show inactive areas on the head of the small lobe. Yellow asterisks indicate no activity was observed in the specific latitude bin, but the area is still interpreted as active overall because it resides in a broadly active sub-region. The blue asterisk in Ma'at 1 indicates that we observed very limited and localized erosion which may be connected to topographic influences. We observed no erosion or deposition within the rest of the region, which may therefore largely behave as a part of the small lobe's hypothesized terminal sink. The red asterisk indicates limited activity, which appears to be the result of settling of sediment due to gravitational instabilities, rather than the direct result of sublimation activity— we therefore interpret the region to be a part of the large lobe's terminal sink extent. (b) A 3D projection of the regions interpreted as active (red) or inactive (blue). The *Z*-axis is shown in blue, the *Y*-axis in green, and the *X*-axis in red. Dashed lines indicate the negative axis direction.

from the surface in August 2015. The result of this activity is a net-zero loss of material on the tops of either lobe across all modeled grain sizes (Lai et al., 2016), consistent with our observations.

Despite the limited observed activity and surface changes, these deposits will likely still evolve thermally. Though the upper centimeters of the surface may be exhausted of their ices, material just below the diurnal skin depth, which has an average value of ∼2 cm on 67P (Jindal et al., 2022), could be especially enriched in volatiles if there is even a small degree of net-deposition to buffer and protect these sediments from sublimating their internal ices.

Given how stationary grains on these surfaces may be, sintering may also add a small degree of cohesion. Not only would this armor the surface against subsequent erosion and re-mobilization of deposited grains, but it may also set up subsurface stratigraphy. Specifically, if mixing and granular convection are small, these deposits may have multiple inter-bedded layers that reflect the deposition of new material across multiple orbits.

We therefore interpret these regions as terminal sinks for sediment, where the small amounts of airfall grains that meet the surface may not be able to subsequently leave, even near perihelion. Sediment would therefore be transport-limited and would instead thermally evolve in situ and more slowly than other smooth terrain deposits over many orbits. Such deposits may therefore retain larger ice volumes than other smooth terrain deposits on 67P, possibly making them high value targets for sample return missions, which aim to collect smooth terrain samples due to the unprecedented characterization of this morphology by Philae's landing. Yet, smooth terrains in these regions still bury the underlying topography. The net-zero activity levels then suggest that these near-polar deposits must accumulate extremely slowly, or that these deposits accumulated in a different "climate" wherein 67P's obliquity was more favorable for a more rapid accumulation. Follow-up sediment transport models should investigate this more rigorously, as well as the potential effects of sintering and the comparative ice depletion of freshly generated versus redistributed sediments in order to understand when these smooth terrains accumulated their sediment and what that implies for 67P's long-term surface and thermal evolution.

4.2. Implications for Other Comets

Of the six resolved comets imaged to date, five were viewed with sufficient resolution to analyze the comets' surface morphology. On all five, we observe that smooth terrains cover a significant fraction of their surfaces. The resolution of images collected in past comet missions has, in many cases, thus far prevented the detection of these processes on other comets. Future research aims to address this question by degrading the resolution of Rosetta images to search for evidence of these processes in lower resolution images from other comet nuclei.

The sublimation-driven processes described above on 67P have both planetary and cometary analogs. Mars's scalloped terrains and swiss cheese terrains (Lefort et al., 2010; Morgenstern et al., 2007), Pluto's pits (Howard et al., 2017), Triton's depressions in its southern hemisphere terrains (Hansen et al., 2021) and hollows on Mercury (R. J. Thomas et al., 2014) all exhibit striking similarities to scarp fronts observed on 67P, wherein volatile sublimation liberates refractory grains, driving the back-wasting of scarps. Scarp retreat is also proposed as a mechanism for the growth of Titan's small lake depressions (Hayes, 2016) and occurs across Earth where failure at a cliff base, combined with efficient transport of the produced sediment, forms a characteristic shape (Howard, 1995). Though significant differences in the dynamics and timescales arise due to the presence of atmospheres on these worlds and different materials and ices, the morphologic similarity between these features on diverse worlds across the solar system remains striking. On comet 9P/Tempel 1, jet activity was spatially linked to a series of migrating scarps on the nucleus (Farnham et al., 2013). Scalloped features have also been seen on comet 9P/Tempel 1 (Veverka et al., 2013; P. C. Thomas et al., 2013a), providing evidence of previous scarp migrations on other comets. Additionally, comet 9P/Tempel 1's S2 "flow" boundary recession (P. C. Thomas et al., 2013a) closely parallels scarp migrations found on 67P, where near surface volatile ices sublimate and cause the recession of a smooth terrain boundary. While the various expressions of scarp migrations described indicate an influence from various planetary conditions (e.g., gravity, volatile-refractory mixing at the grain scale, presence/absence of an atmosphere, etc.), the underlying physics related to how ice sublimation can initialize the mobilization of grains and result in back-wasting scarp fronts is clearly universal across the solar system.

We also speculate that the honeycomb features may be analogous to sublimation features on Mars, such as brain terrain, which form via differential sublimation processes on thermally fractured surfaces (Hu et al., 2017; Mangold, 2003). The small scale and variable expression of honeycombs on 67P could be the result of the highly irregular shape of 67P's surface or due to highly localized subsurface fractures. These may also represent smaller scale textures that exist in larger plains formations, in which case their presence on other comets would depend largely on local topography, and the surface's propensity to fracture. While we have not detected such features on other comet surfaces, such textures may have occurred at scales that were not resolvable. A more detailed study of these features is warranted, as their formation is unique and remains puzzling (Hu et al., 2017).

The process of redistributing smooth terrains via sublimation also likely depends on the physical and compositional parameters of a given comet. Gravity, for example, influences the travel distances of grains and maximum

loftable grain sizes (Steckloff et al., 2021). Therefore, for comets with equal activity levels, we might expect larger nuclei to have more isolated, thicker deposits of smooth terrains with a larger component of fine grains than smaller comets. Further, larger comets could hold on to more ice-depleted materials since smaller particles rapidly lose their ices (Davidsson et al., 2021). We also expect the obliquity of the comet to influence the distribution of smooth terrains. Objects with a 0° obliquity would likely have smaller smooth terrain deposits centered around one or both of their poles and, except regions of gravitational lows, no smooth terrains in the low to mid-latitudes. On the contrary, comets with high obliquity like 67P have larger smooth terrain deposits on the hemisphere that experiences polar winter near perihelion, as re-mobilization at such locations is hampered.

If 67P's orbital parameters were different in the past (Maquet, 2015), the subsolar latitude at perihelion would also be different (Hirabayashi et al., 2016). This would likely alter the locations where smooth terrains net accumulate/erode. These expectations are also consistent with observations of two main regions of smooth deposits observed on comet 9P/Tempel 1, which has gravity ∼1.5 times larger than 67P (Richardson et al., 2007) and an obliquity of 28° (Sekanina, 1981). On comet 9P, we observe one south polar smooth terrain deposit, and two located in gravitational lows (P. C. Thomas et al., 2013a). We also observed smooth terrains within the neck and on the large lobe of Hartley 2 (Bruck Syal et al., 2013). With ∼10 times less gravity than 67P (Jia et al., 2017; Sierks et al., 2015; P. C. Thomas et al., 2013b), these potentially larger grains may be more ice-enriched, explaining their observed activity (A'Hearn et al., 2011; Steckloff et al., 2016).

It is imperative that we address these questions with future landers, orbiters, flybys, and sample return missions. In particular, comet sample return missions can address primary science questions from the past decadal survey (National Academies of Sciences, Engineering, and Medicine, 2022) regarding the formation of comets and the influence of the evolution of the early solar system. One such possible comet sample return mission is CAESAR (Lauretta et al., 2018; Squyres et al., 2018), which plans to collect a sample from the smooth terrains of a JFC. Since we expect the same processes to be influencing the morphology and ice content on other comet nuclei, this work is important to understanding ideal sample locations on either 67P or other nuclei. Because gravity, obliquity, and timing of perihelion should strongly affect the location, distribution and composition of smooth terrains, they are also vital factors to consider when selecting sample sites for possible comet sample return missions.

5. Conclusions

The processes acting on 67P's smooth terrains are driven by the sublimation of volatiles from both the consolidated nucleus and the sediment within the comet's smooth terrain deposits. As the comet approached and passed through perihelion, erosional activity followed the subsolar latitude southward. The primary expression of this erosion is scarp migration, which is mainly limited to low-latitude, external regions and regions where topography provides localized heating due to re-radiation (i.e., neck and lobe-facing regions, pits in Ash 1 and Seth 1). The increase in erosion as 67P approached perihelion led to intra- and inter-regional redistribution of sediment within the smooth terrains. This redistribution confirms that some volatile ices survive the transport process from the consolidated southern hemisphere to the smooth terrain deposits in the north. To sample recently deposited grains sourced directly from the southern hemisphere, collection sites should be selected from more southern smooth terrains where scarp fading and burial can be tracked as indicators of recent deposition (e.g., Imhotep). External regions between ∼30°N and 60°N experience polar winter during perihelion. At these northern extents, near-zero net erosion and deposition occurs. In a slightly net-depositional environment, this may create terminal sinks where any deposited sediment is less able to be removed from the surface in 67P's current orbital configuration. Such terminal sinks represent valuable locations that probe the paleoclimate of 67P. While the expression of the processes driving sediment transport may vary, we broadly expect the processes shaping 67P's smooth terrains to apply to other comets of similar compositions and orbital parameters since smooth terrain erosion appears to be driven largely (but not entirely) by direct solar insolation, although the location of active erosion and deposition, cold trapping regions, and more generally the distribution, redistribution and composition of smooth terrains, will also depend on the comet's mass, and geometry.

Data Availability Statement

All raw images are available on ESA's Archive Image Browser and are credited to ESA/Rosetta/MPS for OSIRIS Team MPS/UPD/LAM/IAA/SSO/INTA/UPM/DASP/IDA—CC BY-SA 4.0 (https://imagearchives.esac.esa.int) under the CC BY-SA 4.0 license. This license text can be found at https://creativecommons.org/licenses/

by-sa/4.0/legalcode. ShapeViewer 4.0.0 software is publicly available for download at www.comet-toolbox.com. ArcMap software is available at https://www.esri.com/en-us/arcgis/products/arcgis-for-personal-use/buy with registration and fee. All relevant shapefiles, layers, and basemaps are available at Cornell University's eCommons (Barrington et al., 2023).

Acknowledgments
This research was supported by a Rosetta Data Analysis Program Grant 80NSSC19K1307 and by the Heising-Simons Foundation (51 Pegasi b Fellowship to S. B.). We would like to acknowledge Bjorn Davidsson, who provided helpful comments on earlier versions of this manuscript. We would also like to acknowledge the Principal Investigator of the OSIRIS camera on ESA's Rosetta spacecraft, Holger Sierks, and the ESA Planetary Science Archive for the data used in this study. This research has made use of the scientific software ShapeViewer (www.comet-toolbox.com).

References

Acton, C. H. (1996). Ancillary data services of NASA's navigation and ancillary information facility. *Planetary and Space Science*, *44*(1), 65–70. https://doi.org/10.1016/0032-0633(95)00107-7

A'Hearn, M. F., Belton, M. J. S., Delamere, W. A., Feaga, L. M., Hampton, D., Kissel, J., et al. (2011). EPOXI at comet Hartley 2. *Science*, *332*(6036), 1396–1400. https://doi.org/10.1126/science.1204054

A'Hearn, M. F., Feaga, L. M., Keller, H. U., Kawakita, H., Hampton, D. L., Kissel, J., et al. (2012). Cometary volatiles and the origin of comets. *The Astrophysical Journal*, *758*(1), 29–36. https://doi.org/10.1088/0004-637X/758/1/29

Barrington, M., Birch, S. P., Jindal, A., Hayes, A. G., Corlies, P., & Vincent, J. B. (2023). Dataset for Quantifying morphological changes & sediment transport pathways on comet 67P/Churyumov-Gerasimenko [Dataset]. Cornell University Library eCommons Repository. https://doi.org/10.7298/52H7-XK42

Barucci, M. A., Filacchione, G., Fornasier, S., Raponi, A., Deshapriya, J. D. P., Tosi, F., et al. (2016). Detection of exposed H_2O ice on the nucleus of comet 67P/Churyumov-Gerasimenko. *Astronomy & Astrophysics*, *595*, A102. https://doi.org/10.1051/0004-6361/201628764

Birch, S. P. D., Hayes, A. G., Umurhan, O. M., Tang, Y., Vincent, J., Oklay, N., et al. (2019). Migrating scarps as a significant driver for cometary surface evolution. *Geophysical Research Letters*, *46*(22), 12794–12804. https://doi.org/10.1029/2019GL083982

Birch, S. P. D., Tang, Y., Hayes, A. G., Kirk, R. L., Bodewits, D., Campins, H., et al. (2017). Geomorphology of comet 67P/Churyumov-Gerasimenko. *Monthly Notices of the Royal Astronomical Society*, *469*(Suppl_2), S50–S67. https://doi.org/10.1093/mnras/stx1096

Britt, D. T., Boice, D., Buratti, B., Campins, H., Nelson, R., Oberst, J., et al. (2004). The morphology and surface processes of Comet 19/P Borrelly. *Icarus*, *167*(1), 45–53. https://doi.org/10.1016/j.icarus.2003.09.004

Brownlee, D. E., Horz, F., Newburn, R. L., Zolensky, M., Duxbury, T. C., Sandford, S., et al. (2004). Surface of young Jupiter family comet 81P/Wild 2: View from the Stardust spacecraft. *Science*, *304*(5678), 1764–1769. https://doi.org/10.1126/science.1097899

Bruck Syal, M., Schultz, P. H., Sunshine, J. M., A'Hearn, M. F., Farnham, T. L., & Dearborn, D. S. (2013). Geologic control of jet formation on comet 103P/Hartley 2. *Icarus*, *222*(2), 610–624. https://doi.org/10.1016/j.icarus.2012.11.040

Davidsson, B. J. R., Birch, S., Blake, G. A., Bodewits, D., Dworkin, J. P., Glavin, D. P., et al. (2021). Airfall on comet 67P/Churyumov-Gerasimenko. *Icarus*, *354*, 114004. https://doi.org/10.1016/j.icarus.2020.114004

Deshapriya, J. D. P., Barucci, M. A., Fornasier, S., Feller, C., Hasselmann, P. H., Sierks, H., et al. (2016). Spectrophotometry of the Khonsu region on the comet 67P/Churyumov–Gerasimenko using OSIRIS instrument images. *Monthly Notices of the Royal Astronomical Society*, *462*(Suppl_1), S274–S286. https://doi.org/10.1093/mnras/stw2530

El-Maarry, M. R., Groussin, O., Keller, H. U., Thomas, N., Vincent, J. B., Mottola, S., et al. (2019). Surface morphology of comets and associated evolutionary processes: A review of Rosetta's observations of 67P/Churyumov–Gerasimenko. *Space Science Reviews*, *215*(4), 36. https://doi.org/10.1007/s11214-019-0602-1

El-Maarry, M. R., Groussin, O., Thomas, N., Pajola, M., Auger, A. T., Davidsson, B., et al. (2017). Surface changes on comet 67P/Churyumov-Gerasimenko suggest a more active past. *Science*, *355*(6332), 1392–1395. https://doi.org/10.1126/science.aak9384

El-Maarry, M. R., Thomas, N., Giacomini, L., Massironi, M., Pajola, M. A. U. R. I. Z. I. O., Marschall, R., et al. (2015). Regional surface morphology of comet 67P/Churyumov-Gerasimenko from Rosetta/OSIRIS images. *Astronomy & Astrophysics*, *583*, A26. https://doi.org/10.1051/0004-6361/20152573

Farnham, T. L., Bodewits, D., Li, J. Y., Veverka, J., Thomas, P., & Belton, M. (2013). Connections between the jet activity and surface features on Comet 9P/Tempel 1. *Icarus*, *222*(2), 540–549. https://doi.org/10.1016/j.icarus.2012.06.019

Fornasier, S., Hasselmann, P. H., Barucci, M. A., Feller, C., Besse, S., Leyrat, C., et al. (2015). Spectrophotometric properties of the nucleus of comet 67P/Churyumov-Gerasimenko from the OSIRIS instrument onboard the ROSETTA spacecraft. *Astronomy & Astrophysics*, *583*, A30. https://doi.org/10.1051/0004-6361/201525901

Groussin, O., Sierks, H., Barbieri, C., Lamy, P., Rodrigo, R., Koschny, D., et al. (2015). Temporal morphological changes in the Imhotep region of comet 67P/Churyumov-Gerasimenko. *Astronomy & Astrophysics*, *583*, A36. https://doi.org/10.1051/0004-6361/201527020

Hansen, C. J., Castillo-Rogez, J., Grundy, W., Hofgartner, J. D., Martin, E. S., Mitchell, K., et al. (2021). Triton: Fascinating Moon, likely ocean world, compelling destination!. *Planetary Science Journal*, *2*(4), 137–148. https://doi.org/10.3847/PSJ/abffd2

Hayes, A. G. (2016). The lakes and seas of Titan. *Annual Review of Earth and Planetary Sciences*, *44*(1), 57–83. https://doi.org/10.1146/annurev-earth-060115-012247

Hirabayashi, M., Scheeres, D. J., Chesley, S. R., Marchi, S., McMahon, J. W., Steckloff, J., et al. (2016). Fission and reconfiguration of bilobate comets as revealed by 67P/Churyumov-Gerasimenko. *Nature*, *534*(7607), 352–355. https://doi.org/10.1038/nature17670

Howard, A. D. (1995). Simulation modeling and statistical classification of escarpment planforms. *Geomorphology*, *12*(3), 187–214. https://doi.org/10.1016/0169-555X(95)00004-O

Howard, A. D., Moore, J. M., White, O. L., Umurhan, O. M., Schenk, P. M., Grundy, W. M., et al. (2017). Pluto: Pits and mantles on uplands north and east of Sputnik Planitia. *Icarus*, *293*, 218–230. https://doi.org/10.1016/j.icarus.2017.02.027

Hu, X., Shi, X., Sierks, H., Fulle, M., Blum, J., Keller, H. U., et al. (2017). Seasonal erosion and restoration of the dust cover on comet 67P/Churyumov-Gerasimenko as observed by OSIRIS onboard Rosetta. *Astronomy & Astrophysics*, *604*, A114. https://doi.org/10.1051/0004-6361/20162990

Jia, P., Andreotti, B., & Claudin, P. (2017). Giant ripples on comet 67P/Churyumov-Gerasimenko sculpted by sunset thermal wind. *Proceedings of the National Academy of Sciences*, *114*(10), 2509–2514. https://doi.org/10.1073/pnas.1612176114

Jindal, A. S., Birch, S. P. D., Hayes, A. G., Umurhan, O. M., Marschall, R., Soderblom, J. M., et al. (2022). Topographically influenced evolution of large-scale changes in comet 67P/Churyumov–Gerasimenko's Imhotep region. *Planetary Science Journal*, *3*(8), 193. https://doi.org/10.3847/PSJ/ac7e48

Keller, H. U., Arpigny, C., Barbieri, C., Bonnet, R. M., Cazes, S., Coradini, M., et al. (1986). First Halley multicolour camera imaging results from Giotto. *Nature*, *321*(S6067), 320–326. https://doi.org/10.1038/321320a0

Keller, H. U., Barbieri, C., Lamy, P., Rickman, H., Rodrigo, R., Wenzel, K. P., et al. (2007). OSIRIS—The scientific camera system onboard Rosetta. *Space Science Reviews*, *128*(1–4), 433–506. https://doi.org/10.1007/s11214-006-9128-4

Keller, H. U., & Kührt, E. (2020). Cometary nuclei—From Giotto to Rosetta. *Space Science Reviews*, *216*(1), 14. https://doi.org/10.1007/s11214-020-0634-6

Keller, H. U., Mottola, S., Davidsson, B., Schröder, S. E., Skorov, Y., Kührt, E., et al. (2015). Insolation, erosion, and morphology of comet 67P/Churyumov-Gerasimenko. *Astronomy & Astrophysics*, *583*, A34. https://doi.org/10.1051/0004-6361/201525964

Keller, H. U., Mottola, S., Hviid, S. F., Agarwal, J., Kührt, E., Skorov, Y., et al. (2017). Seasonal mass transfer on the nucleus of comet 67P/Churyumov–Gerasimenko. *Monthly Notices of the Royal Astronomical Society*, *469*(Suppl_2), S357–S371. https://doi.org/10.1093/mnras/stx1726

Lai, I.-L., Ip, W. H., Su, C. C., Wu, J. S., Lee, J. C., Lin, Z. Y., et al. (2016). Gas outflow and dust transport of comet 67P/Churyumov-Gerasimenko. *Monthly Notices of the Royal Astronomical Society*, *462*(Suppl_1), S533–S546. https://doi.org/10.1093/mnras/stx332

Lauretta, D. S., Squyres, S. W., Messenger, S., Nakamura-Messenger, D., Nakamura, T., Glavin, D. P., et al. (2018). The CAESAR new frontiers mission: 2. Sample science. In *49th lunar and planetary science conference, the Woodlands, TX, contribution number 2083*.

Lefort, A., Russell, P. S., & Thomas, N. (2010). Scalloped terrains in the Peneus and Amphitrites Paterae region of Mars as observed by HiRISE. *Icarus*, *205*(1), 259–268. https://doi.org/10.1016/j.icarus.2009.06.005

Lisse, C. M., Gladstone, G. R., Young, L. A., Cruikshank, D. P., Sandford, S. A., Schmitt, B., et al. (2022). A predicted dearth of majority Hypervolatile ices in Oort cloud comets. *The Planetary Science Journal*, *3*(5), 112. https://doi.org/10.3847/PSJ/ac6097

Mangold, N. (2003). Geomorphic analysis of lobate debris aprons on Mars at Mars Orbiter Camera scale: Evidence for ice sublimation initiated by fractures. *Journal of Geophysical Research*, *108*(E4), 8021–8033. https://doi.org/10.1029/2002JE001885

Maquet, L. (2015). The recent dynamical history of comet 67P/Churyumov-Gerasimenko. *Astronomy & Astrophysics*, *579*, A78. https://doi.org/10.1051/0004-6361/20142541

Marschall, R., Mottola, S., Su, C. C., Liao, Y., Rubin, M., Wu, J. S., et al. (2017). Cliffs versus plains: Can ROSINA/COPS and OSIRIS data of comet 67P/Churyumov-Gerasimenko in autumn 2014 constrain inhomogeneous outgassing? *Astronomy & Astrophysics*, *605*, A112. https://doi.org/10.1051/0004-6361/201730849

Morgenstern, A., Hauber, E., Reiss, D., van Gasselt, S., Grosse, G., & Schirrmeister, L. (2007). Deposition and degradation of a volatile-rich layer in Utopia Planitia and implications for climate history on Mars. *Journal of Geophysical Research*, *112*, E6. https://doi.org/10.1029/2006JE002869

National Academies of Sciences, Engineering, and Medicine. (2022). *Origins, worlds, and life: A decadal strategy for planetary science and astrobiology 2023–2032*. The National Academies Press. https://doi.org/10.17226/26522

Oklay, N., Vincent, J. B., Fornasier, S., Pajola, M., Besse, S., Davidsson, B. J., et al. (2016). Variegation of comet 67P/Churyumov-Gerasimenko in regions showing activity. *Astronomy & Astrophysics*, *586*, A80. https://doi.org/10.1051/0004-6361/20152739

Pajola, M., Oklay, N., La Forgia, F., Giacomini, L., Massironi, M., Bertini, I., et al. (2016). Aswan site on comet 67P/Churyumov–Gerasimenko: Morphology, boulder evolution, and spectrophotometry. *Astronomy & Astrophysics*, *592*, A69. https://doi.org/10.1051/0004-6361/20152785

Pajola, M., Lucchetti, A., Fulle, M., Mottola, S., Hamm, M., Da Deppo, V., et al. (2017). The pebbles/boulders size distributions on Sais: *Rosetta*'s final landing site on comet 67P/Churyumov–Gerasimenko. *Monthly Notices of the Royal Astronomical Society*, *469*(Suppl_2), S636–S645. https://doi.org/10.1093/mnras/stx1620

Reinhard, R. (1986). The Giotto encounter with comet Halley. *Nature*, *321*(S6067), 313–318. https://doi.org/10.1038/321313a0

Richardson, J. E., Melosh, H. J., Lisse, C. M., & Carcich, B. (2007). A ballistics analysis of the Deep Impact ejecta plume: Determining Comet Tempel 1's gravity, mass, and density. *Icarus*, *191*(2), 176–209. https://doi.org/10.1016/j.icarus.2007.08.033

Sekanina, Z. (1981). Rotation and precession of cometary nuclei. *Annual Review of Earth and Planetary Sciences*, *9*(1), 113–145. https://doi.org/10.1146/annurev.ea.09.050181.000553

Shi, X., Hu, X., Sierks, H., Güttler, C., A'Hearn, M., Blum, J., et al. (2016). Sunset jets observed on comet 67P/Churyumov-Gerasimenko sustained by subsurface thermal lag. *Astronomy & Astrophysics*, *586*, A7. https://doi.org/10.1051/0004-6361/201527123

Sierks, H., Barbieri, C., Lamy, P. L., Rodrigo, R., Koschny, D., Rickman, H., et al. (2015). On the nucleus structure and activity of comet 67P/Churyumov-Gerasimenko. *Science*, *347*(6220), 1044. https://doi.org/10.1126/science.aaa1044

Sodorblom, L. A., Becker, T. L., Bennett, G., Boice, D. C., Britt, D. T., Brown, R. H., et al. (2002). Observations of comet 19/Borrelly by the miniature integrated camera and spectrometer aboard Deep Space 1. *Science*, *296*(5570), 1087–1091. https://doi.org/10.1126/science.1069527

Squyres, S. W., Nakamura-Messenger, K., Mitchell, D. F., Moran, V. E., Houghton, M. B., Glavin, D. P., et al. (2018). The CAESAR new frontiers mission: 1. Overview. In *49th lunar and planetary science conference, the Woodlands, TX, contribution number 2083*.

Steckloff, J. K., Graves, K., Hirabayashi, M., Melosh, H. J., & Richardson, J. E. (2016). Rotationally induced surface slope-instabilities and the activation of CO_2 activity on comet 103P/Hartley 2. *Icarus*, *272*, 60–69. https://doi.org/10.1016/j.icarus.2016.02.026

Steckloff, J. K., Lisse, C. M., Safrit, T. K., Bosh, A. S., Lyra, W., & Sarid, G. (2021). The sublimative evolution of (486968) Arrokoth. *Icarus*, *356*, 113998. https://doi.org/10.1016/j.icarus.2020.113998

Steckloff, J. K., Sarid, G., & Johnson, B. C. (2023). The effects of early collisional evolution on Amorphous water ice bodies. *The Planetary Science Journal*, *4*(1), 4. https://doi.org/10.3847/PSJ/aca75a

Sunshine, J. M., Thomas, N., El-Maarry, M. R., & Farnham, T. L. (2016). Evidence for geologic processes on comets. *Journal of Geophysical Research: Planets*, *121*(11), 2194–2210. https://doi.org/10.1002/2016JE005119

Thomas, N., Davidsson, B., El-Maarry, M. R., Fornasier, S., Giacomini, L., Gracia-Berná, A. G., et al. (2015a). Redistribution of particles across the nucleus of comet 67P/Churyumov-Gerasimenko. *Astronomy & Astrophysics*, *583*, A17. https://doi.org/10.1051/0004-6361/20152609

Thomas, N., Sierks, H., Barbieri, C., Lamy, P. L., Rodrigo, R., Rickman, H., et al. (2015b). The morphological diversity of comet 67P/Churyumov-Gerasimenko. *Science*, *347*(6220), aaa0440. https://doi.org/10.1126/science.aaa0440

Thomas, P. C., A'Hearn, M., Belton, M., Brownlee, D., Carcich, B., Hermalyn, B., et al. (2013a). The nucleus of comet 9P/Tempel 1: Shape and geology from two flybys. *Icarus*, *222*(2), 453–466. https://doi.org/10.1016/j.icarus.2012.02.037

Thomas, P. C., A'Hearn, M. F., Veverka, J., Belton, M. J., Kissel, J., Klaasen, K. P., et al. (2013b). Shape, density, and geology of the nucleus of comet 103P/Hartley 2. *Icarus*, *222*(2), 550–558. https://doi.org/10.1016/j.icarus.2012.05.034

Thomas, R. J., Rothery, D. A., Conway, S. J., & Anand, M. (2014). Hollows on Mercury: Materials and mechanisms involved in their formation. *Icarus*, *229*, 221–235. https://doi.org/10.1016/j.icarus.2013.11.018

Tsou, P., Brownlee, D. E., Anderson, J. D., Bhaskaran, S., Cheuvront, A. R., Clark, B. C., et al. (2004). Stardust encounters comet 81P//Wild 2. *Journal of Geophysical Research*, *109*(E12), S01. https://doi.org/10.1029/2004JE002317

Veverka, J., Klaasen, K., A'Hearn, M., Belton, M., Brownlee, D., Chesley, S., et al. (2013). Return to comet Tempel 1: Overview of Stardust NExT results. *Icarus*, *222*(2), 424–435. https://doi.org/10.1016/j.icarus.2012.03.034

Vincent, J.-B., A'Hearn, M. F., Lin, Z. Y., El-Maarry, M. R., Pajola, M., Sierks, H., et al. (2016). Summer fireworks on comet 67P. *Monthly Notices of the Royal Astronomical Society*, *462*(Suppl_1), S184–S194. https://doi.org/10.1093/mnras/stw2409

Vincent, J.-B., Martinez, G. M., Renno, N. O., & Lemmon, M. T. (2018). ShapeViewer, a software for the scientific mapping and morphological analysis of small bodies. In *49th lunar and planetary science conference, abstract #1281*.

Erratum

In the originally published version of this article, the ninth and tenth paragraphs of Section 2, beginning with "In addition to the six broad" and ending with "pits that appear in Ash 1" and beginning with "We classified each type of change into categories of erosion" and ending with "deposition of new smooth terrain sediment" were incorrectly added. In addition, the last sentence in the tenth paragraph of Section 2 was incorrectly added: "Changes within each time bin were compared to the subsolar latitude, which was calculated using SPICE." The figure citation was incorrectly cited as Figure 4 instead of Figure 7 in the first sentence of Section 3.1.2, the first sentence of the second paragraph of Section 3.1.2.1, and the first sentence of the second paragraph of Section 3.1.2.2. All errors have been corrected, and this version may be considered the authoritative version of record.